A numerical study of effective parameters for the retention of a boron carbide particle in an aluminum substrate including a pore in Al/B_4C reinforced particle aluminum matrix composite coatings

by

Hannaneh Manafi Farid

A thesis submitted in partial fulfillment of the requirements for the degree of

Master of Science

Department of Mechanical Engineering
University of Alberta

Abstract

In this thesis, the impact deposition process of a single boron carbide particle on an aluminum matrix with a pore at different depths in a cold sprayed coating is simulated using a three dimensional numerical model. A finite element model within the framework of the Arbitrary Lagrangian Eulerian (ALE) method and two distinct material models (the Gurson-Tvergaard-Needleman model for the aluminum substrate and the Johnson-Holmquist-Beissel model for the boron carbide particle) are used in Abaqus finite element software. The effect of impact velocity, particle size, and pore size and location on the retention parameters including penetration depth, crater morphology, and plastic strain is explored. These parameters exhibit a nonlinear relationship and enhance particle retention synergistically. The effects of pores on strain hardening and particle fragmentation on the substrate are also explained by localized plastic strain on the contact surface. This thesis shows that some porosity in the substrate may improve some particle retention parameters, specifically at low impact velocity when the pore has a significant impact on particle retention. Consequently, the models developed here can guide selection of deposition parameters towards improving material performance in terms of mechanical and tribilogocal properties.

Preface

This thesis titled, "A numerical study of effective parameters for the retention of a boron carbide particle in an aluminum substrate including a pore in Al/B_4C reinforced particle aluminum matrix composite coatings" is an original work by Hannaneh Manafi Farid.

- Part of Chapter 2 of this thesis has been published in the Journal of *"Materials, Special Issue: Advanced Ceramics and Composites: Design, Structure, Processing, Properties, and Applications"* as **H. Manafi Farid**, A. McDonald, and J.D. Hogan, "Journal of Materials, Special Issue: Advanced Ceramics and Composites: Design, Structure, Processing, Properties, and Applications". I was responsible for performing the simulations in this study and the manuscript composition. A. McDonald was the co-supervisory author and was involved with manuscript composition. J.D. Hogan was the supervisory author and was involved with concept formation and manuscript composition.

"Cypresses swing in the storms, but their roots are deep into the earth, and their heads are high among the stars."

-Nazim Hikmet

To all the courageous souls in Iran who are fighting for

"Woman, Life, Freedom"

Acknowledgments

First and foremost, I would like to extend my appreciation and gratitude towards my supervisor, Dr. James Hogan, for his expertise, ideas, insightful discussions, patience, and mentorship throughout every stage of my entire graduate degree. All of his guidance and support has made me a better researcher and has polished my technical skills.

I am also appreciative to my co-supervisor, Dr. André McDonald, for the excellent and insightful discussions, feedback, and ideas at every stage of my research that pushed me beyond my boundaries of critical thinking. Overall, his perspective on my research, constructive criticism, and advice has enabled me to complete my thesis.

Next, the completion of my graduate degree would not have been possible without the support of my fellow comrades at the Centre for Design of Advanced Materials (CDAM). I appreciate the collaboration and encouragement from my group mate Harshil Pisadava. I'm extremely grateful to senior group member Cass Li for taking the time to mentor me through my graduate studies and assisting with the writing and completion of this thesis. I would also like to thank Kasra Rezasefat for his guidance and feedback in numerical modeling.

Finally and above all, I wish to offer my greatest thanks and special gratitude to my mother Azam Jedari Awli and my sister Dr. Reyhane Manafi Farid for their moral support, encouragement, and motivation. Without their long-lasting support, I would not have made it through my Master of Science degree.

This work is supported by InnoTech Alberta (Dr. Gary Fisher), the Major Inno-

vation Fund (MIF) Program with the Grant Number of MIF01, Imperial Oil, the Province of Alberta—Ministry of Jobs, Economy, and Innovation, and the Natural Science and Engineering Research Council of Canada. The views and conclusions contained in this document are those of the authors and should not be interpreted as representing the official policies, either expressed or implied, of InnoTech Alberta, Imperial oil, the Province of Alberta—Ministry of Jobs, Economy, and Innovation or Natural Science and Engineering Research Council of Canada. This research was also enabled in part by support provided by Compute Ontario (www.computeontario.ca/) and Compute Canada (www.computecanada.ca) via the Graham cluster.

Table of Contents

List of Tables

List of Figures

List of Symbols

General material properties

ν Poisson's ratio

ρ Density

E Young's modulus

G Shear modulus

K Bulk modulus

T Yield strength

Geometrical symbols

$D_{Particle}$ Particle diameter

D_{Pore} Pore diameter

$H_{Substrate}$ Substrate height

$R_{Substrate}$ Substrate radius

Gurson-Tvergaard-needleman model parameters

$\dot{\varepsilon}_S$ Equivalent strain rate term of shear stress

$\dot{\varepsilon}_T$ Equivalent strain rate term of yield stress

σ_{eq} Equivalent stress

σ_m Hydrostatic pressure

σ_y Yield stress of material

ε_{ii}^{p} Plastic hydrostatic strain

ε_{eq}^{p} Critical equivalent plastic strain

df Changes in void volume fraction

df_{growth} Void change by void growth

$df_{nucleation}$ Void change by void nucleation

f Void volume fraction

f_u^* Ultimate value of damage parameter

f_* Modified damage parameter and porosity

f_0 Initial void volume fraction

f_c Critical void volume fraction

f_F Void volume fraction at final failure

f_N Volume fraction of void forming particles

q_1, q_2, q_3 Constitutive parameters

S_j Lower bound (j=0) and upper bound (j=1) of shear stress

S_{ij} Deviatoric stress tensor

S_N Standard Deviation

Johnson-Holmquist Beissel model parameters

μ Volumetric strain *1,2* at phase 1 & 2

$\bar{K}_i$ Pressure coefficient (i=1,2,3) at phase 2

σ_1 Intact strength constant

σ_2 Failed material strength constant

σ_f Failure strength constant

σ_{max} maximum intact strength

C	Strain rate constant
D_1	Material damage constant, Johnson-Holmquist-Beissel model
K_i	Bulk modulus (i=1); ith pressure coefficient (i=1,2,3) at phase 1
n	Material damage constant, Johnson-Holmquist-Beissel model
P^*	Dimensionless pressure
P_1	Intact strength constant
P_2	Failed material strength constant
P_f	Failure pressure constant
T^*	Dimensionless hydrostatic pressure
U_f	Internal energy of the failed material
U_i	Internal energy of the intact material

Abbreviations & Acronyms

3D Three-dimensional.

ALE Arbitrary Lagrangian Eulerian.

CEL Coupled Eulerain Lagrangian.

FEM Finite Element Method.

GTN Gurson-Tvergaard-Needleman.

HEL Hugoniot Elastic Limit.

JC Johsnon-Cook model.

JH Johnsn-Holmquist.

JH-1 Johsnon-Holmquist 1.

JHB Johnson-Homquist-Beissel.

PEEQ Equivalent Plastic Strain.

PRAMC Particle reinforced aluminum matrix composite.

PRMMC Particle reinforced metal matrix composite.

SGP Strain Gradient Plasticity.

SPH Smoothed particle hydrodynamic.

Chapter 1

Introduction

1.1 Thesis Motivation

Particle reinforced metal matrix composite (PRMMC) coatings often consist of a ductile matrix (e.g., aluminum alloy [1–7], copper alloy [8–10], nickel alloy [11, 12], and magnesium alloy [13–15]) and reinforcement particles (e.g., ceramics [16, 17], hard metals [18, 19]), for which the final products usually take advantage of the constituent material properties (e.g., high strength, high stiffness, and low weight [1]). Aluminum is the most frequently used metal in the industry because of its high specific strength, great ductility and toughness, and reasonable cost [20, 21], leading to its use as the matrix in particle reinforced aluminum matrix composites (PRAMCs) in recent years [1, 22–27]. On the other hand, ceramics (e.g., SiC [28], Al_2O_3 [27], TiC [29], TiB_2 [30], and B_4C [31]) are often used as reinforcements in PRAMCs because of their favorable properties (e.g., the high hardness, strength, wear resistance, corrosion resistance [32], high melting point, chemical inertness, electrical and thermal conductivity [32]). Among PRAMCs reported in the literature, aluminum-boron carbide (Al/B_4C) coatings [31] are widely used in aerospace [33], automotive [31, 34], nuclear fuel storage [35], and transportation [36] industries due to their tribological properties [35, 37–40], high hardness and stiffness [37], and fatigue resistance [41].

Typical techniques for manufacturing PRAMCs include friction stir [42], squeeze casting [43], stir casting [44], powder compaction [45], and thermal spray [44]. Among

these techniques, the cold spray method [46] has been well adopted to fabricate these coatings which have been considered as alternatives to metal alloys in recent years [47–49]. In the cold spray technique, a pressurized and preheated process gas in a de Laval nozzle accelerates the micron size particles (5-100 μm) to high velocities (300 to 1200 m/s) and impacts on a substrate. To bond to a substrate, particles must travel at speeds exceeding some critical velocity and be plastically deformed [50, 51]. Cold spray technique guarantees the solid state of the particles in PRAMCs without a phase change [50] and reduces the negative effects associated with elevated temperature gas spray in the industry-standard thermal spraying techniques, such as the tensile thermal stress, residual stress [51], material phase transformation [52], oxidation [53], and decarburization [54], because it requires a low deposition temperature. Moreover, thermally-sensitive and dissimilar materials (e.g., ceramics and metals with distinct thermal properties) can be mixed in feedstock during the process [46, 55], which enlarges the space for material and property design.

To improve the mechanical, chemical, and physical properties of cold-sprayed PRAMCs [2, 23, 56–58], manufacturing (e.g., standoff distance, spraying angle, the nozzle features, gas temperature, and gas velocity [51, 59]) and deposition parameters (e.g., particle size, particle shape, particle type, and porosity [31, 60–64]) need to be carefully chosen to achieve better particle retention since the content and distribution of ceramic reinforcements in the coating play an important role in the final properties of PRAMCs [56]. In addition, the porosity in the metal matrix needs to be better controlled to have desirable structures [65] and favorable mechanical, thermal, and electrical properties [66]. Recent experimental research has shown the relationship between the deposition efficiency (or maximum contents) and particle sizes [67–70], and subsequently, the effect of particle reinforcement size on the tribological properties (e.g., wear resistance) of PRAMC coatings [71–75]. For example, Shikalov et al. [76] measured the wear resistance of Al/B_4C with two sizes of B_4C (17 and 75 μm) and found out that finer particles resulted in higher microhardness with the same

adhesion strength as the larger particles in the Al/B_4C coating. Zhao et al. [67] studied the effect of B_4C particle size (5, 11, 25, and 40 μm) on the Al/B_4C deposition efficiency by examining four particle sizes (5, 11, 25, and 40 μm) and found higher microhardness for coatings with B_4C sizes of 11 and 25 μm. In another study, Zhao et al. [68] investigated the effect of Al particle size on B_4C retention and the Al/B_4C hardness. They showed that small-sized Al improves B_4C retention and changes the wear mechanism from adhesive to abrasive wear.

In addition to these experimental studies, research in the literature has also been done to numerically quantify the effect of the deposition parameters (particle size, impact velocity, surface roughness) [77–79] on a single particle impact [77–81] or multiple particle impact [82–84]. The numerical research has primarily focused on finite element simulations using different approaches (Lagrangian [85–89], Coupled Eulerian Lagrangian [83, 90–93], Arbitrary Lagrangian Eulerian [94–101], and Smooth Particle Hydrodynamics [97, 102–104]) for different material models (e.g., Johnson-Cook [105] and Mie-Gruneisen [106]). These numerical studies often aim to understand the influence of the deposition parameters (density, shape, type and impact velocity and angle) on effective parameters of particle retention (e.g., plastic deformation, surface roughness, penetration depth) in metal/metal and metal/ceramic coatings [75, 77, 78, 93, 107, 108]. Overall, these studies are limited in their ability to: (1) model the elastic-plastic behavior of the ceramic particles subjected to a high impact velocity through physically-relevant ceramic models in order to better understand the fracture and fragmentation of the ceramic particles that affect the metallic matrix behavior, and subsequently, particle retention in the composite [56, 76, 79, 108, 109], and (2) model the substrate porosity effect on the ceramic particle retention considering that particles are fragmented after impacting the substrate [39]. This thesis addresses these gaps by utilizing an arbitrary Lagrangian-Eulerian technique and two sophisticated material models (Gurson-Tvergard-Needleman [110] for the Al substrate and Johnson-Holmquist-Biessel model [111] for the B_4C particle) to simulate ceramic par-

ticle deposition on a metallic substrate for the purpose of exploring how the matrix porosity, impact velocity, and particle size affect the effective particle retention parameters (i.e., depth of penetration, crater morphology, matrix plastic strain, and particle damage).

1.2 Thesis Objectives

The objective of this thesis is to better understand the role of reinforcement particles and impact deposition parameters (e.g., porosity and particle velocity) on the behavior of resulting depth of penetration of the particle, crater morphology, and average and localized equivalent plastic strain in the matrix, which are related to particle retention in composite cold sprayed coatings [77, 78, 93, 112]. The primary focus of this thesis is to explore the effect of porosity of a metallic substrate on the simulated ceramic particle behavior in the substrate. This objective is accomplished via finite element modelling of a single particle undergoing dynamic impact loading. The material constitutive models include both phenomenological (e.g., Johnson-Holmquist- type models [111, 113, 114]) and microstructural physics-based (e.g., Gurson-Tvergaard-Needleman method [110]) approaches to describe high pressure, fracture, and strain-rate dependent behavior of ceramic and ductile materials under high strain rate loading. Finite element models (adaptive mesh techniques) [115–117] are used to simulate the large deformation of the substrate and particle [118]. In this thesis, aluminum-boron carbide (Al/B_4C) is chosen given its novelty and recent interests in the literature [39, 67, 68, 71, 76, 119–122]. Abaqus is the platform utilized for numerical studies to analyze the high strain-rate impact behaviors. Numerical models are developed and validated using both experimental and numerical data from the literature [123–126], and research outcomes will explore the effect of porosity and particle size and velocity on important particle retention parameters, including depth of penetration, crater morphology, and average and localized equivalent plastic strain in the deposition process of the cold sprayed Al/B_4C coating.

1.3 Thesis Actions

To accomplish the thesis objectives, the following actions will be taken:

1. Model the deposition process of ceramic particle reinforced metal matrix composites via a numerical approach by simulating a single B_4C particle deposition on an Al substrate that includes a pore with different diameters and depths from the surface of the substrate. The Johnson-Holmquist-Beissel (JHB) model [111] is implemented to describe the fracture and fragmentation of the B_4C particle under high strain rate impact, and the Gurson-Tvergaard-Needleman (GTN) model [110] is used to explain the failure of the Al substrate based on void nucleation.

2. Study the effect of the particle velocity, particle size, pore size, and pore locations on the retention parameters (e.g., plastic strain, surface morphology, penetration depth) and subsequent deposition efficiency of Al/B_4C coatings by simulation of the impact of a B_4C particle on an Al substrate.

3. Investigate pore collapse and matrix failure through change in the deposition parameters (i.e., impact velocity, particle size, pore size, and pore depth) and link their influence to the particle retention of the Al/B_4C coatings using parameters that are important in particle retention (e.g., equivalent plastic strain, penetration depth, and crater morphology).

4. Provide data sets required for further statistical analysis inputs (such as particle size, particle velocity, and pore size) as well as outputs (such as pore collapse, deformation, and depth of penetration of particles in the substrate) via a systematic simulation of ceramic particle impact. These data sets can be used in the future to simulate the deposition process of multiple particles and coating manufacturing.

1.4 Thesis Contributions

The key contributions of this thesis are summarized as follows:

1. Improve the fundamental understanding of the effect of porosity on the retention of the ceramic/metal particles by using a finite element scheme to better define the relationship between deposition parameters (e.g., particle size, impact velocity) and retention parameters (e.g., equivalent plastic strain).

2. Address the gap in understanding the behavior of the ceramic particles under high strain rate impact loading (e.g., elastic and plastic behavior, and damaged strength) and failure behavior of the ductile materials (high plastic deformation, plastic zones, nucleation and growth of voids) by implementing phenomenological and micromechanical material models to accurately detect the material response.

3. Understand the interplay between loading and material characteristics (e.g., mechanical properties, particle size, impact velocity) that improves the use of ceramic materials in cold spray [127] and additively manufactured structures [128].

4. Provide inputs and outputs for future statistical modeling to understand the mechanical behavior of ceramics under high strain rate loading.

1.5 Thesis Structure

The following outlines the structure of this thesis:

- Chapter 1 introduces the motivation for studying a ceramic particle deposition process on a metallic substrate. This chapter further outlines the thesis objectives, actions, contributions and thesis structure.

- Chapter 2 details a study on modeling the impact of a single B_4C particle on an Al substrate to understand the effect of impact velocity, particle size, and matrix porosity on the particle retention and deposition behavior of cold-sprayed Al/B_4C coatings. This study, titled "Impact deposition behavior of Al/B_4C cold-sprayed composite coatings: Understanding the role of porosity on particle retention" has been published in the journal of " Materials, Special Issues: Advanced Ceramics and Composites: Design, Structure, Processing, Properties, and Applications" in March 2023.

- Chapter 3 summarizes the outcomes and implications of the thesis, and outlines the future work and recommendations for modeling.

Chapter 2

Impact deposition behavior of Al/B_4C cold-sprayed composite coatings: Understanding the role of porosity on particle retention

Part of this Chapter has been published as **Hannaneh Manafi Farid**; André McDonald; and James Hogan. *Impact deposition behavior of Al/B_4C cold-sprayed composite coatings: Understanding the role of porosity on particle retention.* Journal of "Materials, special Issues: Advanced Ceramics and Composites: Design, Structure, Processing, Properties, and Applications". (2023)

Author	Contributions
Hanananeh Manafi Farid	Conceptualization, Methodology, Software, Validation, Formal analysis, Writing - Original Draft, Visualization
André McDonald	Writing - Review & Editing, Supervision
James Hogan	Principal investigator, Conceptualization, Writing - Review & Editing, Supervision

2.1 Abstract

This study explores the role of porosity on the impact deposition of a ceramic-reinforced metal-matrix (i.e., Al/B_4C) composite coating fabricated via cold spraying. The Johnson-Holmquist-Beissel constitutive law and the modified Gurson-Tvergaard-Needleman model were used to describe the high strain-rate behavior of the boron carbide and the aluminum metal matrix during impact deposition, respectively. Within a finite element model framework, the Arbitrary Lagrangian-Eulerian technique is implemented to explore the roles of reinforcement particle size and velocity, and pore size and depth on particle retention by examining the post-impact crater morphology, penetration depth, and localized plastic deformation of the aluminum substrate. Results reveal that some degree of matrix porosity may improve particle retention. In particular, porosity near the surface facilitates particle retention at lower impact velocities, while kinetic energy dominates particle retention at higher deposition velocities. Altogether, these results provide insights into the effect of deposition variables (i.e., particle size, impact velocity, pore size, and pore depth) on particle retention that improves coating quality.

2.2 Introduction

Particle-reinforced metal matrix composite (PRMMC) coatings (e.g., Al/B_4C [31], Al/SiC [129], Al/Al_2O_3 [130]) have been widely employed in a variety of applications (e.g., aerospace [33], automotive [31, 34], fuel storage [35, 131, 132], and transportation [36]) because of their favorable tribological properties [35, 37–39], high hardness and stiffness [37], and fatigue resistance [41]. Typical manufacturing methods for PRMMCs include friction stir [42], squeeze casting [43], stir casting [44], powder compaction [45], and thermal spraying [133]. Among these techniques, the cold spray method [46] was recently adopted because of its favorable attributes: (1) the low temperature of the process ensures no phase change in the material [46], (2) mate-

rials with different thermal properties (e.g., ceramics and metals with very different melting points) and morphology can be mixed in the feedstock during the deposition process towards fabricating composite coatings [46], (3) cold spraying does not produce oxidation in the deposited coating [53], and (4) this technique generates lower residual stresses in the final coating when compared to other thermal spray techniques [51]. These features make the cold spray method a unique technique to manufacture composite coatings in order to reduce material consumption and tailor the physical, mechanical, and tribological properties by blending dissimilar materials to provide commercial products for a variety of industrial applications including [51] to repair magnesium parts in aerospace [134], manufacture electro- or thermo-conductive coatings for power electronic circuit boards [135], design of orthopedic devices [134] in biomedical implants [136]. Moreover, cold-sprayed composite coatings are highly appealing because they do not undergo alloying, phase transformation, or thermite reactions during fabrication processes [137].

During the cold spray process, porosity is an indicator of quality because uncontrolled porosity can result in friable structures and, subsequently, poor mechanical properties [65, 84]. In cold spraying, deposition parameters (e.g., temperature and velocity of the gas, standoff distance, and angle of spraying [51]) and particle morphology (size, shape, type of particles) significantly affect the porosity level in the final coating [71]. To date, limited studies have focused on exploring the effect of porosity on the mechanical properties and structural integrity of Al/B_4C coatings [83, 84, 138–140]. In the literature, Zhao et al. [67] systematically investigated the effect of B_4C and Al feedstock particle size on the weight percentage of the B_4C in the cold-sprayed Al/B_4C coating, and they found the optimal particle size for Al and B_4C was 15 μm to maximize the volume fraction of the B_4C particles ($\approx 30\%$), and to achieve maximum deposition efficiency. In the recent study by Zhao et al. [68], they examined the effect of the Al (metal matrix material) particle size on B_4C retention and the tribological properties of an Al/B_4C cold sprayed composite coat-

ing. They found that the smaller Al size facilitated the B_4C retention because of the grain refinement of the coatings, which also improved its wear resistance. In another study, Shikalov et al. [71] studied the tribological behavior of Al/B_4C coatings for different B_4C powder sizes (17 and 75 μm) and volume percentages, and they found that the higher hardness was attributed to the finer particles, and the B_4C size had no effect on the adhesion strength. Moreover, other studies [39, 51] have shown that hard ceramic particles (e.g., B_4C) fragment more after deposition into softer materials (e.g., Al), resulting in interfacial gaps between the particles and substrate, and subsequently, increasing the porosity level. Building on these studies, our efforts in this study aimed at better understanding the role of the matrix porosity (the size and location of pores), particle sizes, and impact velocities on the resulting impact deposition and, by extension, the quality of Al/B_4C coatings (i.e., particle retention [39, 67]).

To study impact deposition processes in cold spray manufacturing, numerical studies can be used to unravel the effects of deposition parameters (e.g., particle size and shape and impact velocity) by realizing different deposition configurations. Various finite element approaches (e.g., coupled Eulerian-Lagrangian (CEL) [90], arbitrary Lagrangian-Eulerian (ALE) [94, 95], and Lagrangian [85]), and material models (e.g., Johnson-Cook [105] and Mie-Gruneisen [106]) have been employed to model impact deposition responses (e.g., bonding strength[141], retention[142], and rebounding times [78]). Through simulations, it has been shown that the increase in particle impact velocity increases the temperature and plastic deformation of the contact area, which has been shown to have an influence on particle retention and final coating strength [93]. For example, Chakrabarty et al. [77, 107] numerically studied deposition and retention of a single ceramic particle on a metallic substrate at different particle densities, velocities, and impact angles, and found that the oblique spray angle, higher density, and velocity of the depositing particles resulted in increasing the jetting region which strengthened the particle retention on the substrate. In another

study, Elkin et al. [78] numerically studied the role of the surface roughness on the retention of irregular-shaped SiC particles by using the Johnson-Cook [105] model and CEL technique and found that irregular particle shapes resulted in less porosity and better retention when compared to spherical particles [98]. In these studies, the material models for the ceramic particles were simple elastic models and so more physically-relevant ceramic models are needed to better understand the fracture and fragmentation [38, 129] of the particles upon impact into the matrix, which will improve our fundamental understanding of the impact deposition processes. This study will address this gap by implementing the Johnson-Holmquist-Beissel model [111], with considerations for the role of matrix porosity on ceramic particle retention.

In this paper, for the first time in the literature on metal-ceramic composites, we investigate the role of particle size and velocity, and matrix porosity on key particle retention parameters (i.e., depth of penetration, crater morphology, matrix plastic strain, and particle damage) during the deposition of a boron carbide ceramic particle into an aluminum matrix with a pore using the finite element approach. The Johnson-Holmquist-Beissel (JHB) [111] and the Gurson-Tvergaard-Needleman (GTN) [110] material models are used for the ceramic particle and aluminum substrate, respectively. We will investigate the effect of particle diameter, impact velocity, pore diameter, and pore location on the particle penetration depth, crater roughness, and plastic deformation across the contact surfaces in the substrate. Altogether, the results generated in this study will provide insights on the role of porosity during impact deposition behavior of Al/B_4C composites (e.g., matrix strain, roughness, and penetration depth) towards better informing improved cold spray deposition parameters and, eventually, material optimization.

2.3 Methodology and Model Configurations

To better understand the three-dimensional impact deposition behavior of the Al/B_4C coating, and the effect of variables for retention of a B_4C particle on an Al matrix

with a pore, a numerical simulation using Abaqus/explicit finite element software is employed. In this study, the ceramic particle and metallic matrix are treated as brittle and ductile materials, respectively, which are subjected to high-strain-rate impact loadings, and appropriate material models are used to analyze their true behavior. Therefore, the failure behavior of the ductile aluminum substrate is modeled using the Gurson-Tvergaard- Needleman (GTN) model because of its ability to account for the plastic deformation and void growth mechanism [143]. The Johnson-Holmquist-Beissel (JHB) model is used to describe the elastic-plastic deformation of the ceramic because it can reasonably capture the strain-rate-dependent mechanical response of the brittle boron carbide under impact loadings [144]. The following subsections lay out the major constitutive equations for the material models, the finite element framework of the Arbitrary Lagrangian Eulerian technique (ALE) [145], and model configurations used in this study.

2.3.1 The Gurson-Tvergaard-Needlman Model

The Gurson-Tvergaard-Needlman (GTN) model is a well-known elastic-plastic micro-mechanical model that accounts for the ductile damage accumulation in terms of void nucleation, growth, and coalescence [146]. The GTN model is based on continuum damage mechanics and introduces a failure criterion [110]:

$$\phi(\sigma, f) = (\frac{\sigma_{eq}}{\sigma_y})^2 + 2q_1 f^* \cosh{(\frac{3q_2\sigma_m}{2\sigma_y})} - (1 + q_3 f^{*2}) = 0, \tag{2.1}$$

where $q_{1,2,3}$ are constitutive parameters, σ_m is the hydrostatic or mean normal stress ($\sigma_m = (\sigma_{11} + \sigma_{22} + \sigma_{33})/3$), σ_{eq} is the Von Mises equivalent stress ($\sqrt{3S_{ij}S_{ij}/2}$), S_{ij} is the deviatoric stress tensor, σ_y is the yield stress, and f^* represents the modified damage parameter and porosity, which is a function of the volume fraction, f, and defined as:

$$f^* = \begin{cases} f & f \leq f_c \\ f_c + \frac{f_u^* - f_c}{f_F - f_c}(f - f_c) & f_c \leq f \leq f_F, \\ f_u^* & f \geq f_F \end{cases} \tag{2.2}$$

where $\frac{f_u^* - f_c}{f_F - f_c}(f - f_c)$ represents the final phase of ductile failure, f_c is the critical void volume fraction, $f_u^* = \frac{q_1 + \sqrt{q_1^2 - q_3}}{q_3}$ is the ultimate damage parameter, and f_F is the final void volume fraction. The rate of the void volume fraction, $df = df_{\text{nucleation}} + df_{\text{growth}}$, is an addition of nucleation ($df_{\text{nucleation}}$) and the void growth (df_{growth}), where:

$$df_{\text{nucleation}} = A_n \mathrm{d}\varepsilon_{eq}^p, \tag{2.3}$$

with

$$A_n = \begin{cases} \frac{f_N}{S_N\sqrt{2\pi}} e^{-0.5(\frac{\varepsilon^p - \varepsilon_N}{S_N})^2} & \text{if } \sigma_m \geq 0 \\ 0 & \text{if } \sigma_m < 0 \end{cases} \tag{2.4}$$

Here, A_n is a function of the void nucleation (f_N), void nucleation generated strain (ε_N), standard deviation of the void nucleation distribution (S_N), and plastic strain (ε^p). Lastly, the void fraction rate due to the void growth is:

$$df_{\text{growth}} = (1 - f)\mathrm{d}\varepsilon_{ii}^p, \tag{2.5}$$

where ε_{ii}^p is the plastic hydrostatic strain. In this paper, parameters for the model are populated from the previous work by the authors [123, 124], and the literature [125], and these parameters are presented later in Section 2.3.3.

2.3.2 The Johnson-Holmquist-Beissel Model

The JHB model is a phenomenological model that describes the failure behavior of brittle materials subjected to large strain, high strain rate, and high pressure [111]. In this study, the JHB model is applied to describe the mechanical behavior of boron carbide (B_4C) particles impacting an Al substrate. Previous studies demonstrated that B_4C shows a sudden loss in strength under high pressure after the Hugoniot

Elastic Limit (HEL) strength is reached [147], for which this behavior can be well captured by the JHB model [148] because it is more physically relevant for our study. In general, this model consists of three main curves [148]: (1) a strength curve for both intact and damaged ceramics, (2) a damage function describing material failure, and (3) a pressure vs. volumetric strain relationship for bulking and phase change. Each of these components are subsequently described.

First, the strength model (von Misses equivalent stress versus pressure) consists of two curves for intact and failed materials. The von Mises equivalent stress, σ, depends on the pressure, P, the dimensionless equivalent strain rate, $\dot{\varepsilon}^*$, where $\dot{\varepsilon}^* = \dot{\varepsilon}/\dot{\varepsilon_0}$ and $\dot{\varepsilon}_0 = 1.0s^{-1}$, and the damage, D. $D = 0$, $0 < D < 1$, and $D > 1$, represent the intact, partially damaged, and fully damaged or failed materials, respectively. The strength model for the intact material ($D < 1$) is defined as:

$$\sigma = \begin{cases} \sigma_i(P+T)/(P_i+T) & -T < P < P_i \\ \sigma_i + (\sigma_{max} - \sigma_i)\{1.0 - exp[-\alpha_i(P - P_i)]\} & P_i < P, \end{cases} \tag{2.6}$$

where $\alpha_i = \sigma_i/[(\sigma_{max} - \sigma_i)(P_i + T)]$. For failed material ($D = 1$), the the strength model is:

$$\sigma = \begin{cases} (\sigma_f/P_f)P & 0 < P < P_f \\ \sigma_f + (\sigma_{max} - \sigma_f)\{1.0 - exp[-\alpha_f(P - P_f)]\} & P_f < P \end{cases} \tag{2.7}$$

where $\alpha_f = \sigma_f/[(\sigma_{max} - \sigma_f)(P_f + T)]$. T, σ_i, σ_f, P_i, and P_f represent the tensile pressure, minimum nonlinear stress of the intact and failed material, and the corresponding pressure at the minimum nonlinear stress of the intact and failed material, respectively. The strain-rate dependent strength for $\dot{\varepsilon}^* > 1$ is:

$$\sigma = \sigma_0(1.0 + C \ln \dot{\varepsilon}^*), \tag{2.8}$$

where σ_0 is the corresponding strength at $\dot{\varepsilon}^* = 1$ obtained from Eq. 2.6 or Eq. 2.7, and C is a dimensionless strain rate constant.

Next, the damage model to describe the material failure is defined as:

$$D = \Sigma(\Delta\varepsilon_p/\varepsilon_p^f), \tag{2.9}$$

where $\Delta\varepsilon_p$ is the increment equivalent plastic strain and ε_p^f is the constant plastic strain defined as $\varepsilon_p^f = D_1(P^* + T^*)^n$, where $P^* = P/\sigma_{max}$, $T^* = T/\sigma_{max}$, and dimensionless D_1 and n are constants.

Lastly, the hydrostatic pressure model is based on the volumetric strain, $\mu = \frac{V_0}{V} - 1 = \frac{\rho}{\rho_0} - 1$. V, ρ, V_0, and ρ_0 are current volume and density, and initial volume and density, respectively. The pressure model with a phase change and before damage ($D < 1$) is defined as:

$$P = \begin{cases} K_1\mu + K_2\mu^2 + K_3\mu^3 & 0 < \mu < \mu_1 \\ & 0 < P < P_1 \\ (\frac{P_2 - P_1}{\mu_2 - \mu_1})\mu + \frac{P_1\mu_2 - P_2\mu_1}{\mu_2 - \mu_1} & \mu_1 < \mu < \mu_2 \\ & P_1 < P < P_2 \\ \bar{K}_1\bar{\mu} + \bar{K}_2\bar{\mu}^2 + \bar{K}_3\bar{\mu}^3 & \mu > \mu_2 \\ & P > P_2 \end{cases} \tag{2.10}$$

where K_1 (bulk modulus), K_2, K_3, $\bar{K}_1$, $\bar{K}_2$, $\bar{K}_3$, and μ_0 are constants. P_1 is the maximum pressure at phase 1 at μ_1 and P_2 is the minimum pressure at the beginning of phase 2 at μ_2. The transition pressure from phase 1 to phase 2 is a linear model. After the material fails (D= 1), bulking occurs, and the change in pressure is added to the Eq. 2.10. For instance, the pressure model for the failed materials ($D = 1$) and $\mu > 0$ is:

$$P = K_1\mu + K_2\mu^2 + K_3\mu^3 + \Delta P, \tag{2.11}$$

where ΔP is the pressure increment showing the material bulking after failure, and it is obtained considering the change in the internal elastic energy:

$$\Delta p = -K_1\mu_f + \sqrt{(K_1\mu_f)^2 + 2\beta K_1\Delta U}, \tag{2.12}$$

where ΔU is the internal elastic energy loss when failure occurs, μ_f is the volumetric compression at failure, and β ($0 \leq \beta \leq 1$) is the fraction of the internal energy loss converted to potential hydrostatic energy.

2.3.3 Impact Deposition Model Configurations

In this study, a three-dimensional (3D) model of a B_4C particle impacting on an Al substrate is modeled in an Abaqus/Explicit framework to systematically study the cold spray impact deposition process of ceramic/metal composites with a pore. The B_4C particle is regarded as deformable with elastic-plastic behavior taken into account, and this is in contrast to the previous models where ceramic particles are assumed to be elastic using isotropic elastic models [77, 78, 108, 149]. Table 2.1 summarizes the JHB constants for the B_4C particle, and these constants are extracted from the previous study by Johnson and Holmquist [126]. In addition, Table 2.2 also summarizes the GTN model constants, which are taken from Sayahlitifi et al. [124] and modified based on the literature [123, 125] to describe the ductile failure of the Al substrate with void growth considered.

Figure 2.1 shows the model geometry used for the numerical impact simulations. This model was inspired by the 3D models of a cold sprayed single particle in the literature [77, 93, 150, 151] and the high velocity impact modeling example in Abaqus [152]. While the B_4C particle has an irregular morphology [153], which results in better retention in the Al matrix and higher reinforcement contents, in this study, the particle shape is assumed to be spherical to simplify the simulation. Ceramic particles with spherical shapes may have a lower reinforcement fraction [62]. However, they are more likely to increase the in-situ hammering effect, which enhances grain refinement and structure density [1]. Owing to the axi-symmetry of the geometries (a cylindrical substrate and a spherical particle) and loading (perpendicular impact of a particle on a substrate), a slice that is the 1/32 of the entire model following [154] is used to reduce the computational time in this study. In Figure 2.1, three sets of

Table 2.1: The parameters of the Johnson-Holmquist-Beissel (JHB) constitutive model used for the B_4C particle [126].

Density	ρ_0 (kg/m^3) = 2508	2c**Elastic constants**	
2c—**Damage constants**	Modulus of Elasticity	E (GPa) = 442	
Damage coefficient	$D_1 = 0.005$	Poisson's ratio	$\nu = 0.162$
Damage exponent	$n = 1.0$	Bulk modulus	K (GPa) = 218
Max failure strain	$\varepsilon^f_{max} = 999.0$	Shear modulus	G (GPa) = 190
2c—**Strength constants**	2c**Pressure constants**		
Hugoniot elastic limit	HEL (GPa) = 0.27	Bulk modulus (phase 1)	K_1 (GPa) = 218
HEL strength	σ_{HEL} (GPa) = 12.29	Pressure coefficient (phase 1)	K_2 (GPa) = 580
HEL pressure	P_{HEL} (GPa) = 7.95	Pressure coefficient (phase 1)	K_3 (GPa) = 0
HEL volumetric strain	$\mu_{HEL} = 0.0335$	Pressure coefficient (phase 2)	$\bar{K}_1$ (GPa) = 307
Hydrostatic tensile strength	T (GPa) = 0.27	Pressure coefficient (phase 2)	$\bar{K}_2$ (GPa) = 41
Intact strength constant	σ_i (GPa) = 5.9	Pressure coefficient (phase 2)	$\bar{K}_3$ (GPa) = 0
Intact strength constant	P_i (GPa) = 5.9	Transition Pressure	P_1 (GPa) = 25
Max intact strength	σ_{max} (GPa) = 12.5	Transition strain (from P_1)	$\mu_1 = 0.092$
Strain rate constant	$C = 0.01$	Transition pressure	P_2 (GPa) = 45
Failure strength constant	σ_f (GPa) = 4.7	Transition strain (from P_2)	$\mu_2 = 0.174$
Failure strength constant	P_f (GPa) = 30.0	Reference strain (phase 2)	$\mu_0 = 0.03$

Table 2.2: The parameters of the Gurson-Tvergaard-Needleman (GTN) model used for the Al substrate [123–125].

q_1	q_2	q_3	f_0	f_c	f_F	f_N	ε_N	S_N
1.5	1	2.25	0.0017	0.02	0.0363	0.0242	0.1	0.1

boundary conditions are applied: (1) along the symmetric axis where all nodes can only move along the Z axis, (2) on all the side surfaces of the particle and substrate where circumferential velocities of all nodes are zero, and (3) at the substrate bottom where all nodes cannot move along the Z-direction. These boundary conditions are consistent with the literature [152].

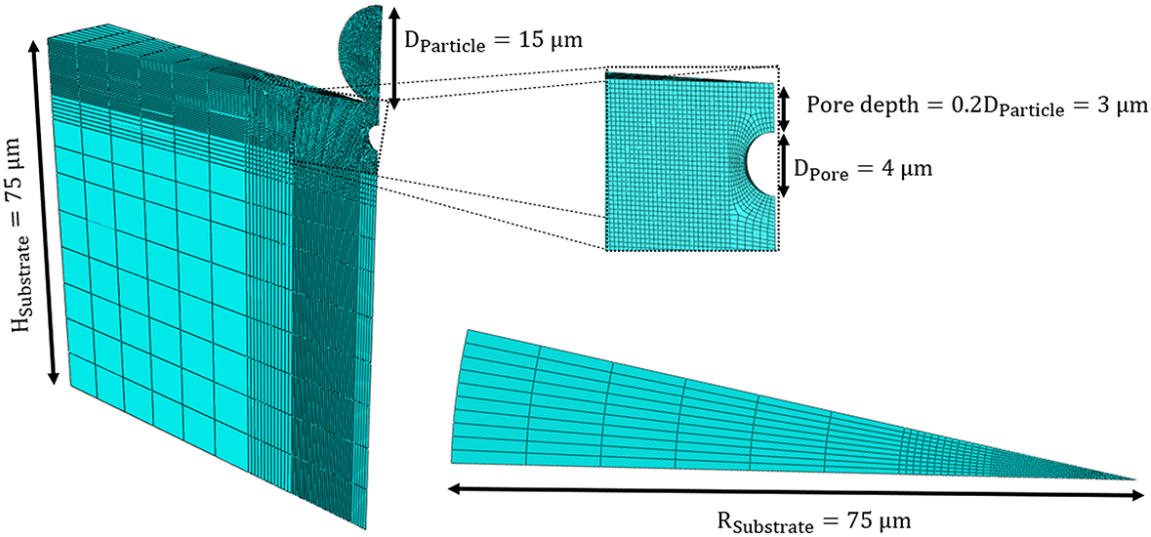

Figure 2.1: Three-dimensional numerical model geometry for simulating a single particle impact during the cold spray deposition process.

In this study, the B_4C particle diameter varies from 15, 25, to 40 µm (Table 2.3), and this is guided by the particle size in experimental studies of Zhao et al. [67]. The substrate height ($H_{Substrate}$) and radius ($R_{Substrate}$) are chosen to be 75 µm to avoid any possible wave reflection (i.e., estimated by using the elastic wave velocity equation, $v = \sqrt{(E/\rho)}$). In this study, simulations are performed over the first 24 ns of impact, which is sufficient to allow for observed behavior to be completed; this also corresponds to before when the elastic wave is reflected from the rear of the substrate to return to the impact zone [155]). In addition, the pore shape is assumed to be spherical to simplify the simulation, and the pore diameters are selected to be 1, 2, 3, and 4 µm. Pore depths are $0.1D_{Particle}$-$0.5D_{Particle}$ based on the observation made in microscopic images of Al/B_4C composites from the literature [38, 39, 67, 71, 81, 129]. Lastly, Figure 2.1 also demonstrates the meshed particle and substrate with

refined areas near the contact region. The mesh size is chosen to be at most 1/50 of the particle diameter near the contact area to avoid element distortion [77, 78, 93]. The friction coefficient is considered to be 0.25 for the contact between particle and substrate, and this is guided by the literature [156]. The interaction between the particle and the substrate is defined using the general contact algorithm, which has been implemented previously in the literature [77, 82, 93]. For employing the ALE method [81], the frequency is set at ten as a default value [81, 101], and the number of remeshing sweeps per increment is set between 5 to 8 for various models in order to avoid errors in analysis [157, 158]. The FS parameter, which is used to minimize the error between numerical and experimental results, is set at 1.5, based on Chalmers [159]. The eight-node linear brick element (C3D8R) with a reduced integration technique and default hourglass is selected for both particle and substrate. The total number of elements for particle and substrate is between 63227 and 155126 elements in the simulations. This type of mesh has also been used in the literature [77, 107, 151]. Compute Canada clusters with one node are used to perform the high-powered parallel computing and minimize the computational time, with a mean run duration of approximately 9 +/- 1 hours per simulation on one node, depending on velocity, particle size, and depth.

Table 2.3: The parameters used for numerical models of the impact deposition simulations in the Abaqus software.

2c—**Dimension parameters**	2c**Modeling parameters**		
Particle Size	15, 25, 40 µm [67]	Analysis framework	Abaqus/explicit
Substrate size	75 µm	FEM technique	Arbitrary Lagrangian Eulerian (ALE)
Pore sizes	1,2,3,4 µm [38, 39, 67, 71, 81, 129]	Interactions	General contact
Depth of pores	0.1 to 0.5$D_{Particle}$ [38, 39, 67, 71, 81, 129]	Friction coefficient	0.25 [156]
Time	24 ns [160]	Element type	C3D8R: An 8-node linear brick [77, 93, 107]
Impact velocity	500, 600, 700 m/s	Mesh design	Reduced integration, hourglass control
		FS	1.5 [159]

2.4 Results and Discussions

Given this study's wide range of numerical data, we classify the results and discussion based on the outputs. Specifically, Sub-Section 2.4.1 compares our model with those in similar studies to verify the model. Sub-Section 2.4.2 describes how the particle penetration depth is affected by deposition parameters (e.g., particle size, impact velocity, and pore sizes and depths). Sub-Section 2.4.3 explores the effect of the pore volume change on the plastic strain of the substrate. Sub-Section 2.4.4 investigates the crater morphology following impact. Sub-Section 2.4.5 examines the pore size and depth on the equivalent plastic strain (PEEQ) value. Next, Sub-Section 2.4.6 investigates the effect of impact velocity, particle size, and pore size on the equivalent plastic strain of the contact surface in the substrate. Finally, Sub-Section 2.4.7 explores results on the localized plastic strain over the contact surface in the substrate. In all areas, we focus on the role of porosity and impact deposition variables (e.g., particle size and velocity) on resulting parameters (e.g., penetration depth, crater roughness, and plastic deformation) that are believed to be associated with particle retention [79, 112].

2.4.1 Model Evaluation

In this sub-section, the predictive capability and accuracy of the model are illustrated through the selection of the mesh size, the trend of accumulation of the equivalent plastic strain (PEEQ) for both substrate and particle, and the PEEQ magnitude compared to the previous studies [77, 93]. In addition, the effect of the particle material type on the plastic strain will be briefly discussed. Prior to presenting these results, it is worth noting that the model developed in this study is challenging to experimentally validate with in-situ deposition data given the small scale of the particles and pores [38, 39, 67, 71, 129], and high speeds of the impact deposition process [39, 71]. Regardless, we attempt to demonstrate how our model aligns with

previous published works.

First, Figure 2.2 compares normalized computational time and the number of elements across different mesh sizes: 0.2, 0.3, 0.4, and 0.5 μm. We use this plot to inform about the tradeoffs between the number of elements and computational time for physically-relevant mesh sizes, as previously done in the literature [77, 93, 112]. We employ the ALE technique, an adaptive meshing tool, to avoid excessively distorted elements and the analysis stops. In the ALE technique, the mesh exposed to excessive distortion is replaced by a mesh domain, whose nodes are placed in the interior of the mesh domain, reducing the overall distortion of the material. However, the mesh nodes and material points lose their correspondence at each re-meshing time, which causes an error in the final results showing the material behaviors [161]. In this case, the mesh convergence analysis, one of the most effective methods to validate a finite element model, is inaccurate [46]. Therefore, mesh sensitivity analysis is not beneficial to validate this model. Instead the method that we used here to validate the model compromises between the element numbers (capturing the relevant physics based on literature [78, 93, 162]) and computational time, which has been used in the literature to compare the different numerical methods (e.g., CEL, ALE, and Lagrangian) to show the efficiency and accuracy of the models [93]. It is worth noting that each numerical FE technique can simulate a different aspect of the cold spray deposition process [82]. The ALE technique provides high precision and is mainly used in the literature [81, 101] to simulate the buildup process of coatings and multi-particle impacts [96]; considering its advantages, we will also use the ALE technique here for further analysis in the future.

To validate the model, the selected mesh sizes are 0.2, 0.3, 0.4, and 0.5 μm [78, 93, 162], which are also employed in the cold sprayed model in the literature. These mesh sizes are implemented for a particle diameter of $D_{Particle}$= 15 μm at the contact areas of the particle and substrate, and near the pore in the substrate. Specifically, these mesh sizes are chosen to be at most 1/50 of the particle diameter (i.e., $\leq$ 0.3

μm) guided by the literature [77, 79, 112] in order to reduce mesh sensitivity of the model. It is observed from Figure 2.2 that at the mesh size of 0.3 μm (with the normalized computational time of 0.148 and the normalized number of elements of 0.991), the number of elements and the associated computational time are notably lower than mesh sizes of 0.2 μm (with the normalized computational time of 2.163 and the normalized number of elements of 2.431). In contrast, the computational times are comparable between the mesh size of 0.3 and 0.4 μm. In conclusion, a refined mesh size of 0.3 μm is chosen in this study for contact areas to balance the accuracy and computational costs [77, 93, 112].

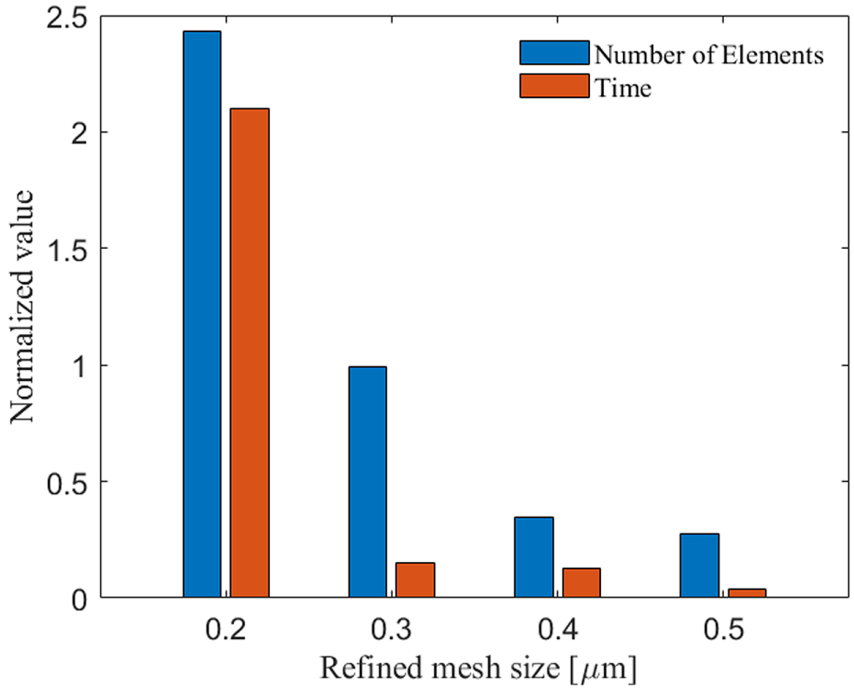

Figure 2.2: Number of elements and computational time for different refined mesh sizes (0.2, 0.3, 0.4, and 0.5 μm) using an ALE FEA framework at the particle-matrix contact areas.

Next, Figure 2.3 shows the PEEQ value over the contact-surface of the substrate and the particle simulated in this study and compared with similar models in the literature [93, 107]. We compare this to determine if our implementation produces results of similar magnitudes and trends to those published in the literature concerning the impact deposition of ceramic particles into metal substrates [77–79, 82, 93]. In

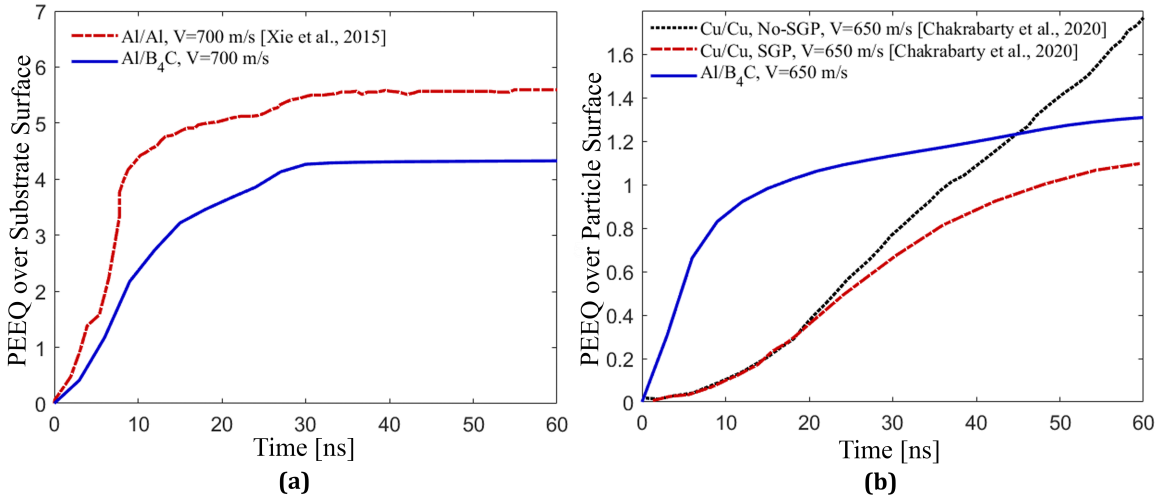

Figure 2.3: Comparison between the equivalent plastic strain (PEEQ) generated in the B_4C particle and the Al substrate in this study and previous studies involving Al and Cu particles and Al and Cu substrates [93, 107]. (**a**) The average PEEQ value over the Al contact-surface in an Al/B_4C coating in the current study (Al/B_4C, V = 700 m/s) and in Al/Al coating reprinted from the literature [93] (Al/Al, V = 700 m/s) with $D_{Particle}$ = 25 µm and V_{Impact} = 700 m/s is calculated using an Arbitrary Lagrangian–Eulerian (ALE) and Coupled Eulerian–Lagrangian (CEL) technique, respectively, in Abaqus. The GTN material model in the current study and the original Johnson–Cook (JC) model in the literature [93] are employed. (**b**) The average PEEQ value over the entire B_4C particle in Al/B_4C using the JHB model (Al/B_4C, V = 650 m/s) and ALE technique, and over the entire Cu particle in Cu/Cu coating using the modified Johnson–Cook (JC) model with and without consideration of strain gradient plasticity (Cu/Cu, SGP, V = 650 m/s and Cu/Cu, No-SGP, V = 650 m/s) and CEL technique as reprinted from reference [107]. The calculations are performed with $D_{Particle}$ = 41 µm and V_{Impact} = 650 m/s.

Figure 2.3a, the PEEQ value over the Al contact-surface in our Al/B_4C coating in the current study and in Al/Al coating reprinted from the literature [93] with a particle diameter of 25 μm and impact velocity of 700 m/s shows that the plastic strain of the Al substrate in this simulation is comparable to previous studies [93]. The solid line in Figure 2.3a represents the PEEQ value over the Al contact-surface for the Al/B_4C cold sprayed coating in this study. For this simulation, the Arbitrary Eulerian-Lagrangian (ALE) method is employed to study the deposition behavior of the particle. The dashed lines represent the PEEQ value over the Al contact-surface in the substrate of Al/Al coating simulated using the Coupled Eulerian Lagrangian (CEL) technique reprinted from the study by Xie et al. [93]. The PEEQ curve trends are similar, and there is no further accumulation of PEEQ after about 30 ns for both coatings (Al/B_4C and Al/Al). This may be due to strain hardening caused by the high velocity impact on the substrate [112]. However, particle material types (ceramic, B_4C, in Al/B_4C and metal, Al, in Al/Al) account for the difference in PEEQ values [93]. The degree of particle ductility influences particle deposition in the cold spray process, since the high velocity impact of softer materials results in additional thermal softening [93], leading to larger plastic deformation, especially at the edges of the deformed particle. Conversely, hard particles (e.g., B_4C) do not thermally soften and are likely to spall at the edges as a result of high impact velocity and pressure waves [160]. Therefore, softer or more ductile materials contribute more to mechanical interlocking than harder ones [79]. Figure 2.3b compares the PEEQ value over the entire B_4C particle in the Al/B_4C coating (in this study) with the PEEQ value over the entire Copper (Cu) particle in the Cu/Cu coating reprinted from reference [107] and shows consistency of two distinct material models: the JHB model and modified Johnson-Cook (JC) model with strain gradient plasticity (SGP). In these two simulations in Figure 2.3b, the particle diameter is 41 μm, the impact velocity is 650 m/s, and the numerical techniques are Coupled Eulerian-Lagrangian (CEL) for Cu/Cu and Arbitrary Lagrangian-Eulerian (ALE) for Al/B_4C. The trend

of the average PEEQ over B_4C particle using the JHB model is analogous to that of the average PEEQ over the Cu particle using the modified JC model with SGP, demonstrating the consistency between the modified JC with the SGP effect and the JHB material model. This is attributed to the inclusion of the plastic strain rate effect in these two models, which is more representative of dynamic impact loading cases [163–165]. Figure 2.3b also shows that the B_4C deformation rate in the Al/B_4C coating is higher than the Cu deformation rate in the Cu/Cu coating, which can be attributed to different particle types and material models. High velocity impacts of harder materials (i.e., B_4C here) result in greater plastic deformation, which enhances the retention of particles [93, 166]. As a result, the JHB model and other models, including the strain-rate-dependency model, play an important role in understanding the mechanical response of materials during impact deposition.

2.4.2 Effect of Pore Size, Particle Size, and Impact Velocity on Penetration Depth

This sub-section will explore the effect of particle size, impact velocity, and pore size on the particle penetration depth. Here, the deeper penetration depth increases the chance of mechanical interlocking; therefore, this is important to quantify in order to better understand particle retention behaviors during deposition into a substrate [77].

Figure 2.4 shows the penetration depth of the center of the substrate during deposition of a single B_4C particle on an Al substrate within 24 ns of impact in order to explore the effect of impact velocities (Figure 2.4a), particle sizes (Figure 2.4b), pore sizes (Figure 2.4c), and pore-to-particle-size ratio (Figure 2.4d) on the penetration depth. In Figure 2.4a with a fixed particle diameter (15 μm) and a range of velocities (500, 600, and 700 m/s) impacting on an intact substrate without a pore, deeper penetration occurs for the higher impact velocities. This is well aligned with the numerical results for different impact velocities in the literature [78] since the higher

impact velocities result in greater kinetic energy that is the main driver of particle retention in the cold spray technique [46]. Figure 2.4b shows results with a fixed impact velocity (500 m/s) and different particle sizes (15, 25, and 40 μm), and results show that deeper penetration occurs for larger particle sizes, as expected, given the greater kinetic energy [46]. For implementation in manufacturing, the deeper particle penetration increases the contact surfaces between particle and substrate, thereby enhancing the chance of mechanical interlocking of the particle and improving particle retention in the substrate [77].

Figure 2.4c shows the combined effect of both pore sizes (1, 2, 3, and 4 μm) and impacting velocities (500, 600, and 700 m/s) on the penetration depth with a pore embedded at a depth of $0.4D_{Particle}$ into the substrate. The particle size is taken as $D_{Particle}$= 15 μm. The pore depth of $0.4D_{Particle}$ is selected based on the literature [39, 71] because there is no noticeable change in behavior for penetration depths in the range of $0.4D_{Particle}$ to $1D_{Particle}$, while no clear trend is observed for the range of $0.1D_{Particle}$ to $0.3D_{Particle}$. In Figure 2.4c, it is observed that higher impact velocities result in deeper penetrations in all cases with different pore diameters, and this is expected due to higher kinetic energy [46], and numerically demonstrated in the literature [78] that the higher impact velocities of the SiC particle result in deeper penetrations. In addition, the effect of including the pore on the penetration depth at higher velocities (i.e., 600 and 700 m/s) is minor. Specifically, the penetration depth for all considered pore diameters is approximately 4 and 5 μm at impact velocities of 600 and 700 m/s, which are close to the penetration depth for the cases without a pore from Figure 2.4a. Conversely, at the lower impact velocity of 500 m/s, the inclusion of pores has a noticeable influence on the penetration depth compared to the higher impact velocities. Namely, at V_{Impact}= 500 m/s, the penetration depth for different pore diameters except for a pore with D_{Pore}= 1 μm is generally more than 4 μm, with no obvious trends for the 2 and 3 μm sizes for ranging impact velocities. This is likely related to the complex interplay of particle comminution

[39], matrix plastic deformation [167], pore crushing and tamping effect [51], and wave mechanics [160] occurring at these small length scales and short time scales in this single particle impact process. Finally, the particle penetrates nearly twice as much as the case without a pore (see Figure 2.4a) or the case with a pore diameter of 1 μm (see Figure 2.4a). Overall, it is believed that the impact velocity has a more significant influence on penetration and is more controllable during cold spray than the pore diameter because of the importance of higher kinetic energy on retention of the particles [46].

Lastly, Figure 2.4d presents results on the effect of a pore with D_{Pore}= 4 and 8 μm at a depth of $0.4D_{Particle}$ from the surface with different particle sizes: 15, 25, and 40 μm to show the effect of different pore-to-particle-size ratio on the penetration depth. As before (Figure 2.4b), the larger particles result in deeper penetrations, and this is believed to be related to greater kinetic energy [46]. In Figure 2.4d, The penetration depth curves for the pore-to-particle-size ratio of particle diameters of 25 and 40 μm do not plateau at the truncated time of the simulation (i.e., t = 24 ns), indicating that larger particles will penetrate deeper for a longer period. The penetration depth increases from 2 in Figure 2.4b to 4.2 μm in Figure 2.4d for the pore-to-particle-size ratio of 0.27 ($\frac{D_{Pore}}{D_{Particle}} = \frac{4}{15}$), increases from 5 to 8 μm for the pore-to-particle-size ratio of 0.16 ($\frac{D_{Pore}}{D_{Particle}} = \frac{4}{25}$), increases from 6.5 to 8 μm for the pore-to-particle-size ratio of 0.1 ($\frac{D_{Pore}}{D_{Particle}} = \frac{4}{40}$), and increases from 6.5 to 10 μm for the pore-to-particle-size ratio of 0.2 ($\frac{D_{Pore}}{D_{Particle}} = \frac{8}{40}$) in Figure 2.4d. These results show that a higher pore-to-particle-size ratio causes deeper particle penetration (the pore-to-particle-size ratio of 0.27 has a maximum penetration depth increase of approximately $\frac{4.2}{2}$ times). In this study, pore-to-particle-size ratios equal to or less than 0.16 have a limited influence on the penetration depth. To the authors' best knowledge, no studies have investigated the effect of the pore-to-particle-size ratio on particle retention. However, the SEM images in the literature [39, 67, 71, 129] show larger pore sizes for larger particles and smaller pores for relatively smaller particle diameters. The results suggest that the

ratio of the pore to particle size should be considered in manufacturing the porous structure using cold spraying [82].

2.4.3 Effect of Change in Pore Volume on the Equivalent Plastic Strain

This sub-section will explore the effect of the pore volume change on the PEEQ value toward better understanding its effect on particle retention [51]. Figure 2.5 illustrates the typical time-evolving changes in pore morphology and the values of PEEQ on the contact-surface in the substrate during the impact of a particle with $D_{Particle}$= 15 μm at V_{Impact}= 500 m/s on a substrate including a pore with D_{Pore}= 4 μm at a depth of $0.3D_{Particle}$. This figure is shown to better understand the pore volume change during the deposition, and its effect on the PEEQ value, with numerical conditions motivated by literature [51, 64]. Figure 2.5a shows the average PEEQ value over the contact-surface in the substrate, indicating the maximum average PEEQ value is 6, which is used in the following figures. Figure 2.5b - f are the time-resolved still frames corresponding to the different time stamps (5, 10, 15, 20, and 24 ns), and these are chosen to demonstrate the pore morphology, the crater morphology, and the PEEQ value over the Al contact-surface during pore collapsing. At a time of t = 5 and 10 ns (Figure 2.5b and c), the pore is collapsing as the PEEQ value over the Al contact-surface is increasing, particularly near the crater edges, and jetting begins to happen at t = 10 ns at the crater edges. However, the PEEQ value is lower than the contact-surface average PEEQ value of 6. Figure 2.5d shows that the pore at time of t = 15 ns is not completely collapsed, and the crater edges demonstrate a higher PEEQ value than the crater center, as well as a larger amount of plastic deformation or jetting. The pore collapses at approximately 17 ns, which is determined by tracking the volume of the pore through time. At t= 20 ns in Figure 2.5e, the pore has already collapsed, and the PEEQ value has increased to 6.9, which is higher than the average PEEQ value of 6 (see Figure 2.5a). Increasing the PEEQ value without changing

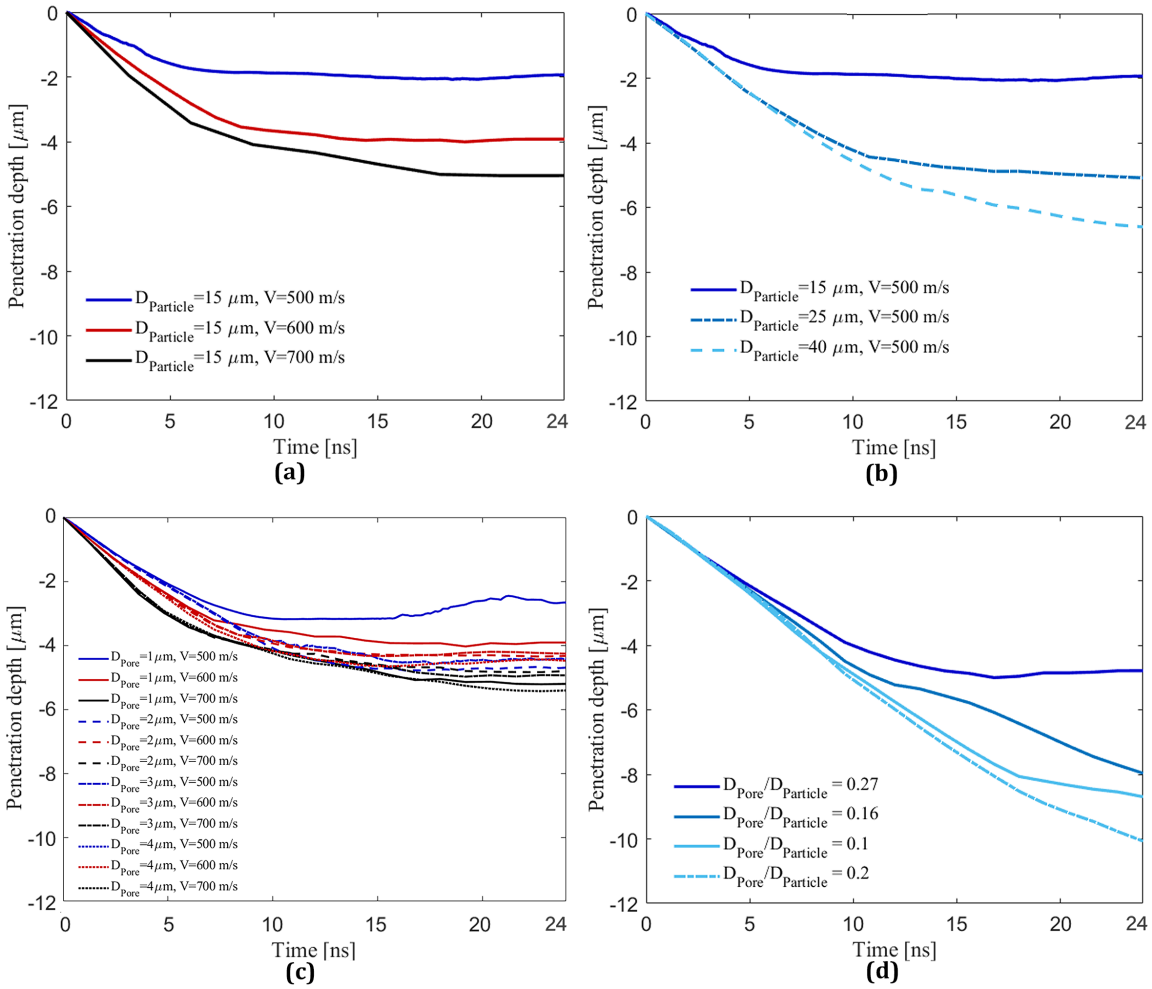

Figure 2.4: The penetration depth of the B_4C particle in an Al substrate vs. time for varying impact velocities, particle size, and pore sizes: (**a**) The penetration depth of the particle with $D_{Particle}$= 15 μm for V_{Impact}= 500, 600, and 700 m/s. (**b**) The penetration depth of the particles with $D_{Particle}$= 15, 25, and 40 μm and V_{Impact}=500 m/s. (**c**) The penetration depth vs. time for $D_{Particle}$= 15 μm at V_{Impact}= 500, 600, and 700 m/s on the substrate including a pore with D_{Pore}= 1, 2, 3, and 4 μm placed at a depth of $0.4D_{Particle}$. (**d**) The penetration depth of particle with $D_{Particle}$= 15, 25, and 40 μm and V_{Impact}= 500 m/s on the substrate with D_{Pore}= 4 and 8 μm placed at a depth of $0.4D_{Particle}$. The curves associated with $\frac{D_{Pore}}{D_{Particle}}$ of 0.27, 0.16, 0.1, and 0.2 correspond to $\frac{D_{Pore}}{D_{Particle}} = \frac{4}{15}$, $\frac{4}{25}$, $\frac{4}{40}$, and $\frac{8}{40}$, respectively.

the pore morphology improves the particle retention in the Al substrate because the kinetic energy converts to plastic deformation energy at the contact-surface rather than changing the pore morphology, which will be discussed in detail in subsequent figure descriptions. Finally, Figure 2.5f shows a further increase in PEEQ value across the Al contact surface, particularly near the crater edges, while the crater morphology, specifically at the crater edges, does not change. This plateauing behavior can be related to the saturation in strain hardening at the contact surface of the particle due to the high impact velocity [112]. More specifically, high impact velocities promote the plastic deformation of the matrix, resulting in surface hardening through the tamping effect that leads to the collapse of the interfacial gaps, flaws, and surface porosity, as well as strengthens the bonding at the metal/ceramic interfaces [51, 168].

2.4.4 Effect of Pore Size, Particle Size, and Impact Velocity on Crater Morphology

Next, we explore the effect of particle size, impact velocity, and pore size on the crater morphology. Surface morphology and its roughness is an effective parameter for improving particle retention [77, 78]. Figure 2.6 illustrates the side and top views of the impact crater at different configurations regarding substrates, pore sizes, and impact velocities at a fixed particle diameter (i.e., 15 μm) and time (i.e., t = 24 ns). Also, the PEEQ vs. time curve for impact velocities of 500 and 700 m/s demonstrates the maximum average PEEQ value over the crater surface used in this figure to determine the distribution of the PEEQ. Figure 2.6a shows the Al substrate crater morphology without a pore at an impact velocity of 500 m/s. A smooth crater without any discontinuous bump across the crater is observed with a graduate increase in PEEQ value towards the crater center. In addition, the PEEQ value at the center is higher than the averaged PEEQ value, indicating localized plastic deformation and stronger bonding at the crater center, as discussed in the literature [79]. As explained in Figure 2.4, the penetration depth is lower for the case without a pore compared to

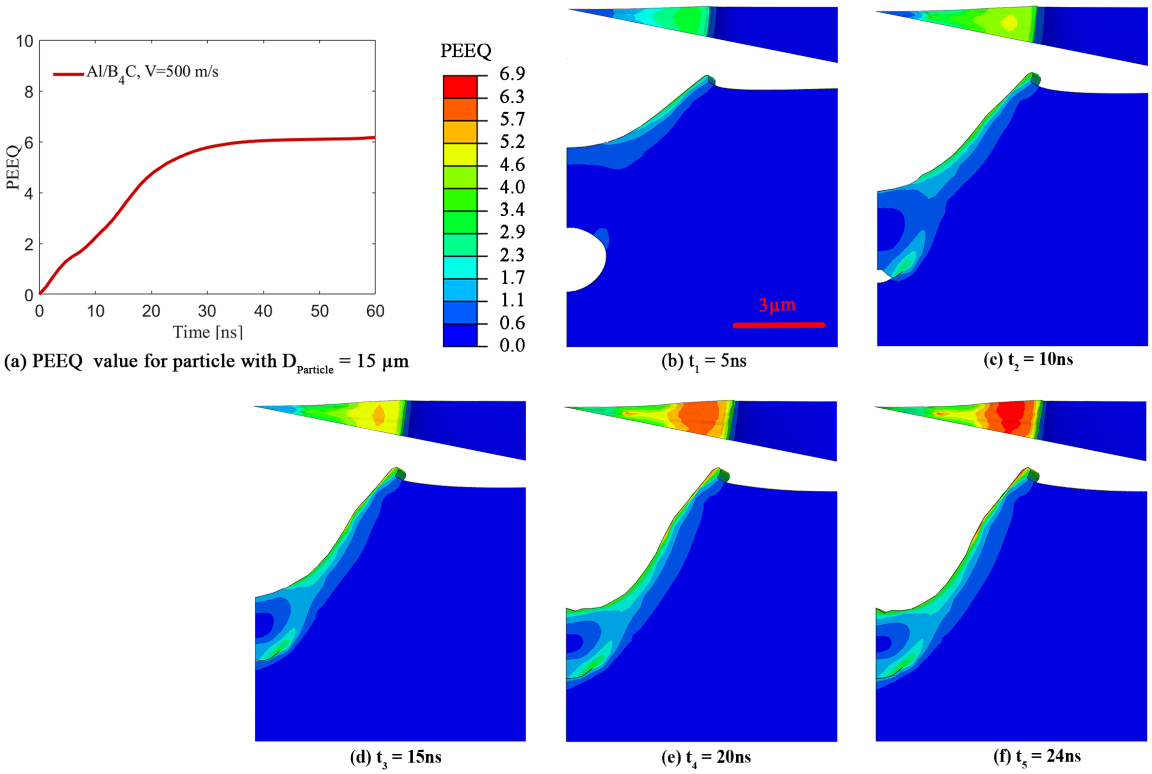

Figure 2.5: The time-resolved still frames showing pore morphology behavior and PEEQ values for a pore with D_{Pore}= 4 µm at a depth of $0.3D_{Particle}$ and V_{Impact}= 500 m/s. (**a**) The average PEEQ value vs. time to determine the maximum PEEQ value which is 6. The top view and the side view of the substrate with a pore are demonstrated at a time range of (**b**) 5 ns, (**c**) 10 ns, (**d**) 15 ns, (**e**) 20 ns, and (**f**) 24 ns in order to show pore volume changes.

the other cases containing a pore, which applies for all sub-figures here. In Figure 2.6b with D_{Pore}= 1 μm at a depth of $0.3D_{Pore}$ and V_{Impact}= 500 m/s, the deformation at the crater edges is similar to the case without a pore (Figure 2.6a), and the crater center displays higher plastic strains, which is in agreement with the literature [79]. In Figure 2.6c, d, and e, the crater shapes from the side views are more non-uniform and uneven, and the crater edges are distorted. The higher PEEQ value is found at the edges of the crater rather than its center for the cases with complete (Figure 2.6c or d) or partial (Figure 2.6e) pore collapses. The severe plastic deformation at the crater edges or jetting [160, 169] occurs in the cases containing a pore with a diameter greater than 1 μm (i.e., Figure 2.6d, e, and f) compared to Figure 2.6a and b. The jetting implies that the particle localized fragmentation occurs at the crater edges and results in material flowing near the crater edges, which has also been shown in literature [160]. Specific particle fragmentation and material flow behaviors will be further explored in Sub-Section 2.4.7. Figure 2.6f shows a substrate that includes a pore with a diameter of D_{Pore}= 4 μm at a pore depth of $0.4D_{Particle}$ at V_{Impact}= 700 m/s, with the saturation of plastic deformation (illustrated as gray color) with PEEQ values of 8.6 being observed across most of the contact surface. Comparing the crater deformation in Figure 2.6f and Figure 2.6a without a pore at $V_{Impact} = 500$ m/s reveals that the substrate material expands more at the crater edges, the deeper penetration occurs at the crater center, and there is a bump near the middle of the crater, which is attributed to the higher impact velocity and higher kinetic energy generation [112, 160]. Altogether, these results are important because they show that, generally, a pore in the substrate significantly contributes to particle deposition. Specifically, the partial or complete pore collapse results in a deeper penetration (see Figure 2.4) and also leads to the non-uniform crater shapes (see Figure 2.6) of the contact-surface and excessive distortion of the crater edges (see Figure 2.5 and 2.6). The pore effect on the crater morphology and deeper penetration can facilitate improved mechanical interlocking, subsequent particle retention, and finally, increased deposition efficiency

of ceramics in the coating [77, 78, 160].

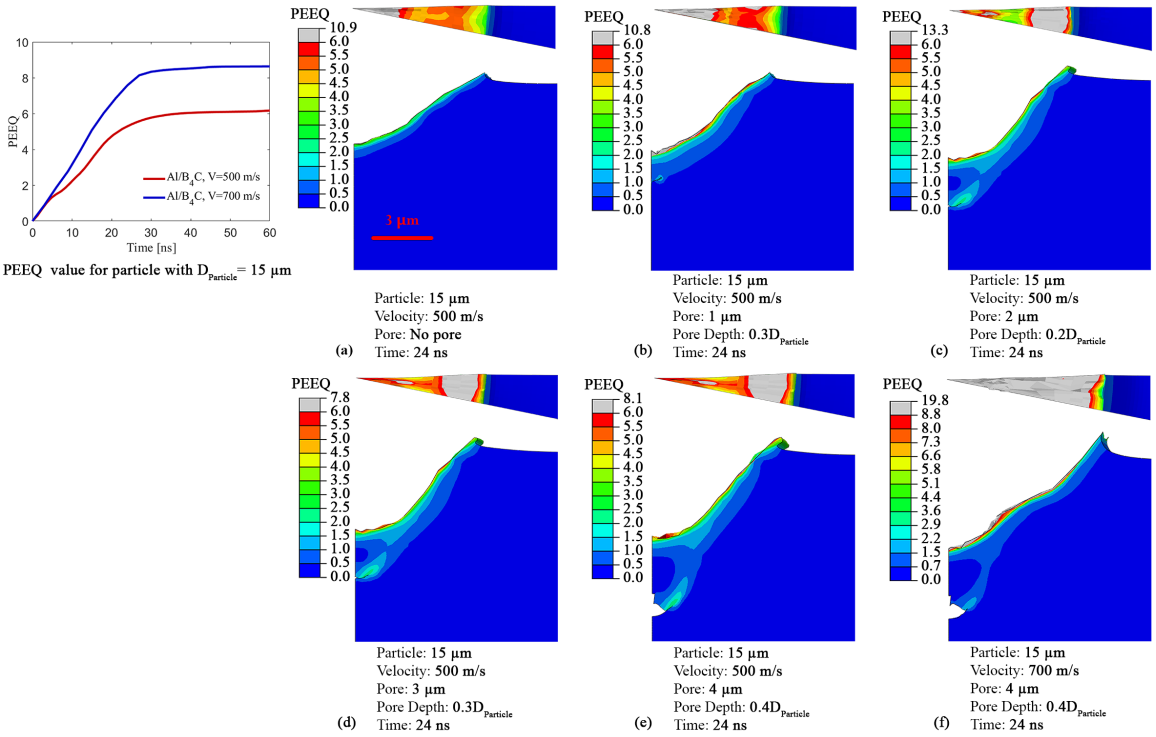

Figure 2.6: Comparison of the substrate crater morphology for $D_{Particle}$= 15 µm cases of: (**a**) Without pore and V_{Impact}= 500 m/s. (**b**) With pore of D_{Pore}= 1 µm at a depth of $0.3D_{Particle}$ and V_{Impact}= 500 m/s. (**c**) With pore of D_{Pore}= 2 µm at a depth of $0.2D_{Particle}$ and V_{Impact}= 500 m/s. (**d**) With pore of D_{Pore}= 3 µm at a depth of $0.3D_{Particle}$ and V_{Impact}= 500 m/s. (**e**) With pore of D_{Pore}= 4 µm at a depth of $0.4D_{Particle}$ and V_{Impact}= 500 m/s. (**f**) With pore of D_{Pore}= 4 µm at a depth of $0.4D_{Particle}$ and V_{Impact}= 700 m/s.

2.4.5 Effect of Pore Size and Depth on the Time-evolved Equivalent Plastic Strain

In this sub-section, we explore the effect of pore size and depth on the average PEEQ value over the contact surface in the substrate at an impact velocity of 500 m/s, motivated by deposition conditions from the literature [51]. The PEEQ value indicates the contact-surface's plastic deformation, which contributes to the localized softening of a thin (few micrometers) layer of the metallic substrate and ceramic particles, leading to enhanced mechanical interlocking [112, 170].

Figure 2.7 demonstrates the PEEQ value over the crater surface of a substrate without a pore and with a pore of different diameters (2, 3, and 4 μm) placed at different depths ($0.1D_{Particle}$ to $0.5D_{Particle}$) from the surface at a fixed particle diameter (15 μm) and impact velocity (500 m/s) within 24 ns of impact to examine the effect of pore diameter and depth on the PEEQ value over the Al contact surface. Figure 2.7 shows the pores with the diameter of 1 and 2 μm have no clear trend on the PEEQ value over the Al surface, which is in contrast to the general trend observed for pore diameters of 3 and 4 μm. For example, a pore with D_{Pore}= 2 μm at different depths slightly affects the PEEQ value compared to the PEEQ value of a substrate without a pore (see solid orange line). On the other hand, a pore with D_{Pore}= 3 and 4 μm significantly impacts the PEEQ value before approximately 17.5 ns, which is denoted in the figure as t*, and defines a time for comparative purposes across all tests after which PEEQ increases linearly at more-or-less the same rate across all conditions. At t^*, the amount of PEEQ value increases, and the particle stops penetrating deeper, which is also demonstrated in Figure 2.5 and described in Sub-Section 2.4.2. This behavior can be attributed to the strain hardening that occurs at the contact-surface in the substrate at this time (between 15 and 20 ns) due to the peening effect of a hard particle on the deformable substrate, which both improves the tribological properties of the surface [73, 171] and increases the PEEQ value, facilitating particle retention [112]. The impact of hard ceramic particles on a metallic matrix reduces the interfacial gaps between the matrix and particles and flattens the metallic matrix due to large plastic deformation. This helps the metallic matrix remain soft, which improves the retention of the ceramic particles (specifically the smaller size) in the matrix [61, 172–174], increasing the deposition efficiency, and by association, the tribological and mechanical properties of the coatings [175].

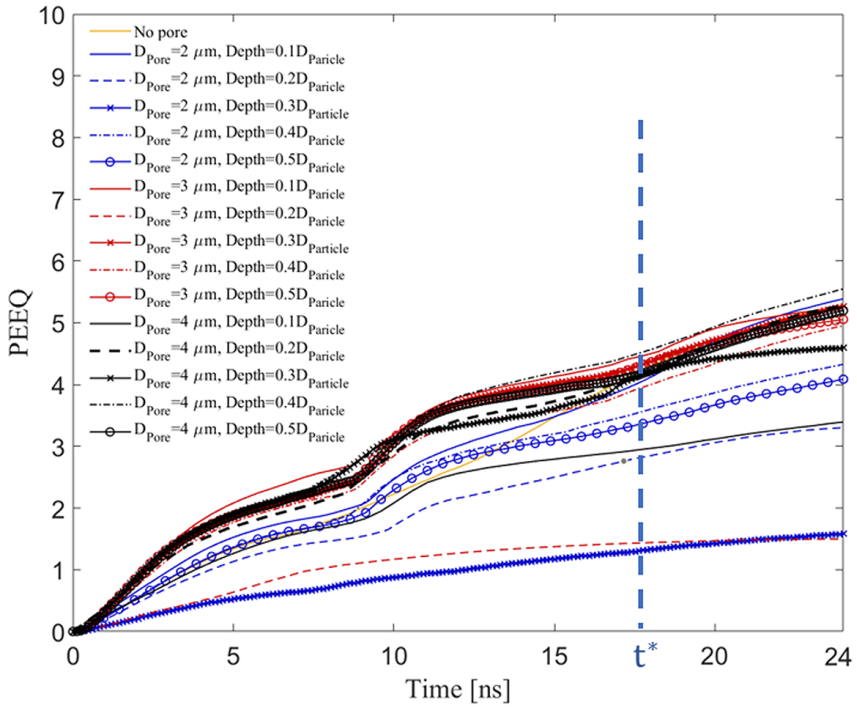

Figure 2.7: The equivalent plastic strain (PEEQ) over the contact-surface of the Al substrate and B_4C particle for $D_{Particle}$= 15 µm and V_{Impact}= 500 m/s with a pore with diameters: D_{Pore}= 2, 3, and 4 µm, placed at different depths from the surfaces ($0.1D_{Particle}$, $0.2D_{Particle}$, $0.3D_{Particle}$, $0.4D_{Particle}$, and $0.5D_{Particle}$). t* in the figure defines a time for comparative purposes across all tests after which the PEEQ increases linearly at more-or-less the same rate across all conditions.

2.4.6 Effect of Impact Velocity, Particle Size, and Pore Size on Time-evolved Equivalent Plastic Strain

In this sub-section, the effect of impact velocity, particle size, pore size (at a fixed depth of $0.4D_{Paericle}$), and particle-to-pore-size ratio on the PEEQ value over the contact surface in the substrate will be further explored to quantify their effects on the PEEQ value, an indicator of particle retention [46, 70, 82, 93, 149]. Figure 2.8 shows the time-evolved PEEQ over the Al substrate for different simulations to investigate the effects of impact velocities (Figure 2.8a), particle sizes (Figure 2.8b), pore sizes (Figure 2.8c), and pore-to-particle-size ratios (Figure 2.8d). Figure 2.8a demonstrates the average PEEQ value measured over the Al contact-surface of three simulations with a fixed particle diameter of 15 μm and different impact velocities (500, 600, and 700 m/s) to examine the effect of impact velocities on an Al substrate without a pore. From Figure 2.8a, there is a correlation showing the higher PEEQ values for higher impact velocity. Increasing the velocity generates more kinetic energy, which results in higher plastic strain and causes a higher plastic-strain-rate over the contact surface in the substrate [176].

In Figure 2.8b, we present the effect of particle sizes ($D_{Particle}$= 15, 25, and 40 μm) at a fixed impact velocity (500 m/s) on the PEEQ value to examine the particle size effect. We observe a correlation between particle diameters and PEEQ values, where the smaller particles are associated with a higher PEEQ value. The particle with $D_{Particle}$= 15 μm has a higher PEEQ than the particle with $D_{Particle}$= 25 μm, and $D_{Particle}$= 25 μm has a higher PEEQ value than the particle with $D_{Particle}$= 40 μm. While this observation may be in contrast to the fact that larger particles with larger masses result in higher kinetic energies, experimental studies in the literature [67] have shown the deposition efficiency of B_4C with $D_{Particle}$= 15 μm in an Al substrate is higher than the deposition efficiency corresponding to particles with $D_{Particle}$= 25 and 40 μm. Other studies [56, 129, 166, 177, 178] have also shown non-intuitive relationships between particle size and velocity on impact deposition. While

still challenging to unravel, our results show consistency between the PEEQ value of different particle sizes and the retention of the particles in experimental observations [67], indicating that determination of optimum particle size and velocity can be attributed to the PEEQ value or the plastic strain deformation over the substrate contact surface. To better understand the particle size effect on the PEEQ value, the evolution of localized plastic strain across the contact surface is explored later in Sub-Section 2.4.7.

Next, Figure 2.8c shows the PEEQ value over the contact-surface of an Al substrate containing a pore with a diameter of 1, 2, 3, and 4 μm placed at a depth of $0.4D_{Particle}$ with a fixed particle diameter of 15 μm and impact velocities of 500, 600, and 700 m/s. By comparing Figure 2.8a and 2.8c, the PEEQ value increases from 5.8 in Figure 2.8a to 6.0 in Figure 2.8c, indicating that higher PEEQ values correspond to higher impact velocities, as expected. Three more important conclusions can be drawn from Figure 2.8c. First, a pore of any diameter affects the PEEQ value in a nonuniform pattern at a lower impact velocity (500 m/s); a pore causes an increase then a decrease in the PEEQ value within 24 ns of deposition. Second, a pore significantly increases the PEEQ value at higher impact velocities (600 and 700 m/s). However, the relationship between the pore diameter and the increase in PEEQ value does not follow a predictable pattern. Three, comparing Figure 2.8c and Figure 2.4c, the effect of including a pore in the substrate on penetration depth (see Figure 2.4c and d) is greater than the effect of including a pore on the increase in PEEQ value (see Figure 2.8c), which might be related to the conversion of kinetic energy into penetration rather than plastic deformation and an increase in PEEQ.

Lastly, Figure 2.8d further explores the effect of the ratio between the pore and particle size on the PEEQ values for different particle diameters of 15, 25, and 40 μm and pore diameters of 4 and 8 μm placed at a depth of $0.4D_{Particle}$ at a fixed impact velocity of 500 m/s. In Figure 2.8d, the curves associated with $\frac{D_{Pore}}{D_{Particle}}$ of 0.27, 0.16, 0.1, and 0.2 correspond to the $\frac{D_{Pore}}{D_{Particle}} = \frac{4}{15}$, $\frac{4}{25}$, $\frac{4}{40}$, and $\frac{8}{40}$, respectively.

Comparing Figure 2.8b with Figure 2.8d shows that the pore-to-particle-size ratio influences PEEQ slightly. Moreover, the increase in PEEQ value for different pore-to-particle-size ratios does not follow a predictable pattern; for example, the PEEQ value for the pore-to-particle-size ratio of 0.2 ($\frac{D_{Pore}}{D_{Particle}} = \frac{8}{40}$) increases by $\frac{3.9}{2.1}$ times at 17.5 ns, which is the most significant increase in PEEQ value compared to the other cases. Overall, the comparison between Figure 2.8d with Figure 2.4d reveals that the effect of including a pore in the substrate on PEEQ is notably less than the effect of including a pore on the penetration depth, recognizing both penetration depth and PEEQ are important for particle retention [51].

2.4.7 Effect of Pore Size, Particle Size, and Impact Velocity on the Localized Equivalent Plastic Strain in the Substrate

This final sub-section examines the effect of impact velocity, particle size, and pore size on the localized PEEQ value across the contact-surface in the substrate towards linking the effect of plastic strain localization on particle retention [112]. Here, localized PEEQ vs. normalized distance along the substrate surface is plotted to investigate the effects of impact velocity (Figure 2.9), particle size (Figure 2.10), and pore size (Figure 2.11). First, Figure 2.9 investigates the effect of impact velocity on localized PEEQ over the Al contact surface without a pore at a fixed particle diameter of 15 μm. The figure shows the time-evolved localized plastic deformation (PEEQ value) over the Al contact-surface along the distance spanning the particle diameter ($2R$) at impact velocities of 500, 600, and 700 m/s and at fixed times (i.e., t = 5, 10, 15, 20, and 24 ns). The substrate PEEQ values at times of 5 and 10 ns at the impact velocity of 500 m/s and at the time of 5 ns at an impact velocity of 600 m/s have a maximum value near the crater edges of the Al substrate (at 0.6 particle radius). This PEEQ behavior is similar to the PEEQ curve trend of the Al substrate in the Al/Al coating from the literature [93], where the PEEQ curve peaks near the edges.

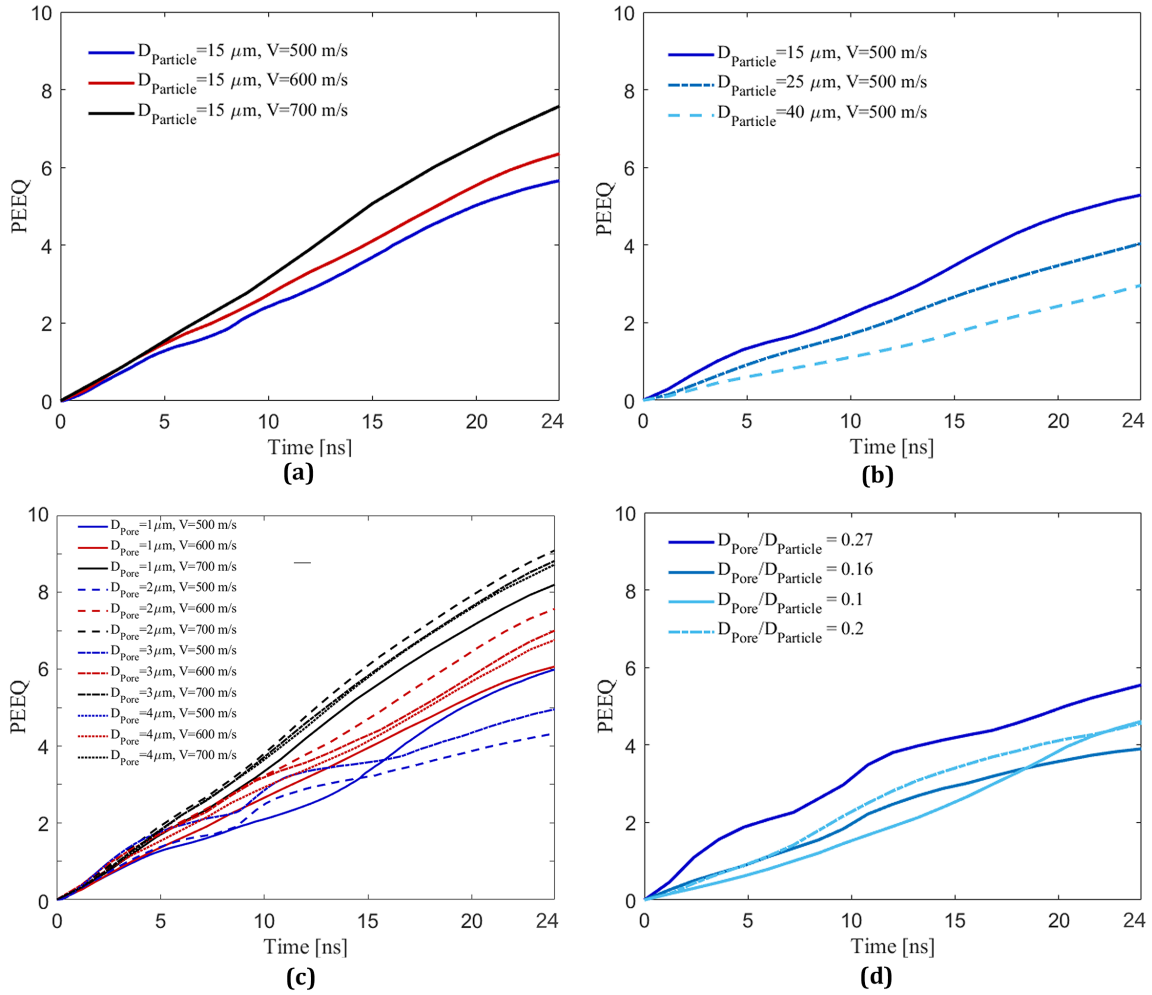

Figure 2.8: Time-evolved equivalent plastic strain (PEEQ) over the contact-surface between the Al substrate and the B_4C particle in the Al substrate. (**a**) Particles with $D_{Particle}$=15 μm and V_{Impact}= 500, 600, and 700 m/s. (**b**) Particles with $D_{Particle}$= 15, 25, 40 μm and the V_{Impact}= 500 m/s. (**c**) $D_{Particle}$= 15 μm and V_{Impact}= 500, 600, and 700 m/s with a pore of D_{Pore}= 1, 2, 3, and 4 μm placed at a depth of $0.4D_{Particle}$. (**d**) Particles with $D_{Particle}$= 15, 25, and 40 μm and V_{Impact}= 500 m/s impacting on a substrate including a pore with diameters of D_{Pore}= 4 and 8 μm placed at a depth of $0.4D_{Particle}$. The curves associated with $\frac{D_{Pore}}{D_{Particle}}$ of 0.27, 0.16, 0.1, and 0.2 correspond to $\frac{D_{Pore}}{D_{Particle}} = \frac{4}{15}, \frac{4}{25}, \frac{4}{40}$, and $\frac{8}{40}$, respectively.

Figure 2.9 at the V_{Impact}= 500 m/s also illustrates the sudden increase in PEEQ value near the crater center after 10 ns in the Al/B_4C coating. In Figure 2.9, the maximum PEEQ value is observed near the crater center and also near the crater edges ($0.6R$) at V_{Impact} = 600 and 700 m/s. Although the localized plastic strain trend is analogous at impact velocities of 600 and 700 m/s, the PEEQ value is different, and the higher PEEQ value corresponds to the higher impact velocity.

The abrupt increases in PEEQ value in Al/B_4C observed here can be attributed to the distinct material types of the particle and substrate. When a harder ceramic particle (B_4C) impacts a softer metallic substrate (Al), its kinetic energy transforms into plastic deformation by a cushioning mechanism, and the matrix surface acts as a cushion and is largely deformed to provide a place for the ceramic particles to retain [167]. This embedment mechanism causes localization of the plastic deformation across the crater surface [51, 93, 167], leading to fracture and fragmentation of the ceramic at the center [51]. The high plastic deformation at the center creates a strong bonding between particle and matrix and facilitates particle retention, as reported for the ceramic/metal coatings in the literature [79]. The discontinuous high PEEQ value at the crater edges stems from the intense pressure wave [70, 179] causing jetting at the crater edges and enhancing the fragmentation and the flow of the comminuted ceramic particles [56]. Hence, we conclude that the B_4C particle impact on the Al substrate results in a maximum PEEQ value near the crater center at all impact velocities and another maximum PEEQ value near the crater edges at higher impact velocities where the comminuted ceramic flow is more visible [79].

Next, Figure 2.10 examines the effect of the B_4C particle size on the localization of the plastic strain over the contact-surface in the Al substrate by demonstrating the PEEQ value vs. the distance per particle radius (Distance/R) across the surface in the substrate for particles with diameters of 15, 25, and 40 μm at a fixed impact velocity (500 m/s) and a substrate without a pore at a range of times (5, 10, 15, 20, 24 ns). In Figure 2.10, an abrupt increase in PEEQ values is observed near the crater

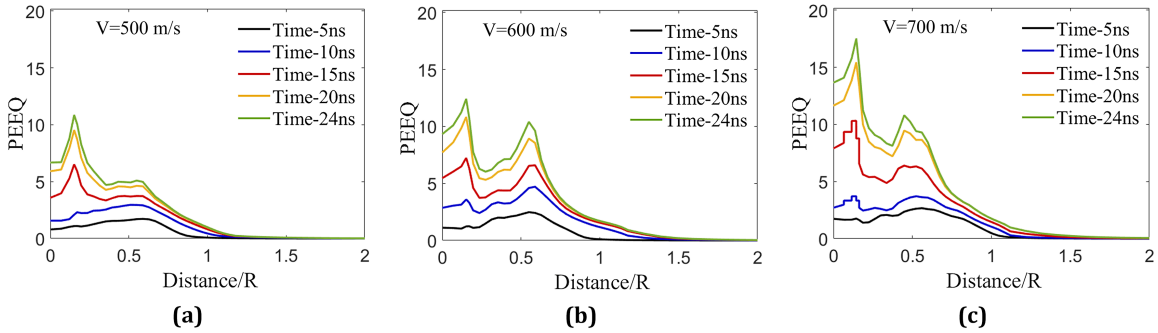

Figure 2.9: The time-evolved localized plastic deformation (PEEQ) over contact-surface between the Al substrate and the B_4C particle in the Al surface. The particle size is $D_{Particle}$=15 μm and impact velocities of 500, 600, and 700 m/s on the Al substrate without pores.

center at the impact of a particle with diameters of 15, 25, and 40 μm on a substrate. These three sub-figures show that the maximum PEEQ value near the center is higher for larger particles (the maximum magnitude corresponds to the particle with $D_{Particle}$= 40 μm). In contrast, the PEEQ value dramatically decreases after its sudden increase, resulting in a lower average PEEQ value for larger particles (see Figure 2.8b), subsequently, lower particle retention, and lower deposition efficiency according to experimental data [67]. A concentration of plastic strain occurs at the center of the crater due to the high kinetic energy of impact, and the rate of deformation increases more rapidly than in the rest of the substrate, which requires more energy and stress to deform. Meanwhile, a more considerable amount of kinetic energy is released at the beginning of the particle deposition and converted into a high plastic strain, whereas there is no further stress or energy to cause another significant localized plastic strain; this is known as strain hardening [31]. Consequently, the lower average PEEQ value for larger particles can be attributed to the strain hardening phenomenon at the crater center, resulting in a considerable localized plastic strain and a significant decrease in PEEQ across the contact-surface in the substrate without an increase [31].

Finally, Figure 2.11 explores the effect of a pore in an Al substrate subjected to the different B_4C impact velocities on the localized plastic deformation (PEEQ) over

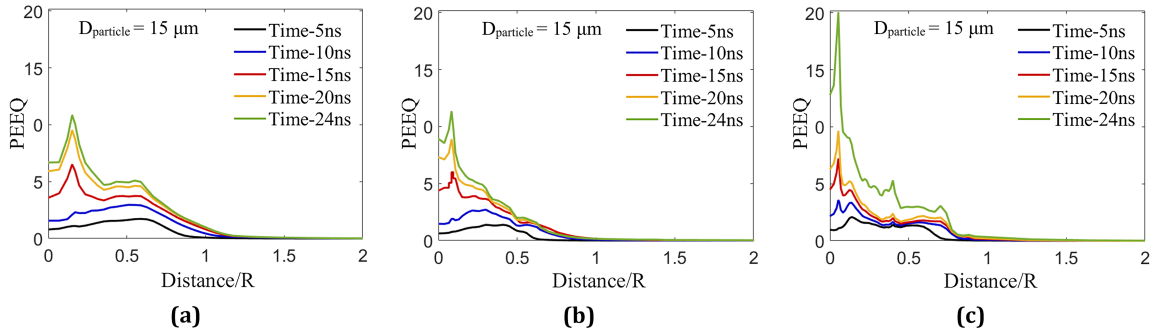

Figure 2.10: The time-evolved localized plastic deformation (PEEQ) over the contact-surface between the Al substrate and the B_4C particle in the Al substrate for different particle diameters of: 15, 25, and 40 μm at a fixed impact velocity (500 m/s) on the Al substrate without a pore.

the contact-surface in the Al substrate. Figure 2.11 consists of three sub-figures showing the PEEQ value vs. the distance per particle radius (Distance/R) across the substrate surface at the time of 24 ns, when the particles stop penetrating deeper (see Figure 2.4c). The particle diameter is fixed ($D_{Particle}$= 15 μm) and the particle velocities are 500, 600, and 700 m/s, and the Al substrate includes a pore with D_{Pore}= 1, 2, 3, and 4 μm at a depth of $0.4D_{Particle}$. In Figure 2.11, at V_{Impact}= 500, 600, and 700 m/s, the PEEQ curve trend and value of the cases containing a pore with $D_{Particle}$= 1 μm are almost identical to those of the cases without a pore, indicating the minor effect of the pore with D_{Pore} = 1 μm on the PEEQ localization and magnitude, as shown in Figure 2.4. Also, there is no trend in the localized plastic strain for the cases with pore diameters of 2, 3, and 4 μm. Nevertheless, the PEEQ value tends to suddenly increase at $0.6R$ near the crater edges, as well as at $0.2R$ near the crater center, similar to Figure 2.9 for the substrate without a pore subjected to the impact velocities of 600 and 700 m/s. However, higher impact velocities result in higher PEEQ values in Figure 2.11, which has already been noted many times previously. Additionally, the sudden increase in PEEQ values near the crater center for the cases containing a pore with D_{Pore}= 2, 3, and 4 μm shifts toward the peak PEEQ value near the crater edges, and this can be related to the existence of a pore at the center.

Overall, in these sub-figures, the localized PEEQ value near the crater center results in fracture and fragmentation of the B_4C particle. The comminuted particles cause a secondary impact and the subsequent rebound of the B_4C particles, leading to a lower deposition efficiency [56]; however, Huang et al. [39] experimentally showed that the fragmented B_4C particles are mechanically interlocked at the crater center in the substrate due to the large plastic deformation and deeper indent of the crater, and Chakrabarty et al. [79] proved this using smoothed-particle hydrodynamics method. In addition, the particle fragmentation, spall-like processes, and the flow of the comminuted particles at the crater edges can be attributed to the maximum PEEQ value near the crater edges. Overall, our results show that the inclusion of a pore promotes damage and fracture in the ceramic particle, leading to larger plastic deformation and, subsequently, enhanced retention [51]. This brings new considerations for designing and manufacturing cold-sprayed coatings, especially those with inherent porosity and under lower-speed deposition rates [82, 180].

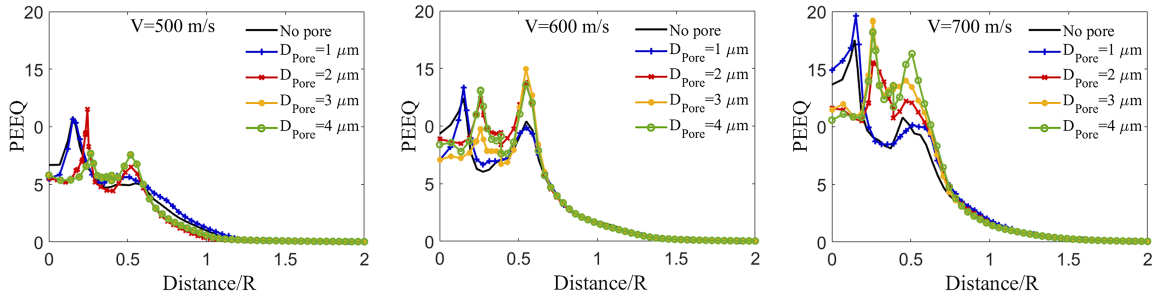

Figure 2.11: The time-evolved localized plastic deformation (PEEQ) over the contact-surface between the Al substrate and the B_4C particle with $D_{Particle}$= 15 μm in the Al substrate with a pore (D_{Pore}= 1, 2, 3, and 4 μm) at a depth of $0.4D_{Particle}$ at the impact velocities of 500 m/s, 600 m/s, and 700 m/s. These results are taken at 24 ns after impact for comparative purposes, with 24 ns being a time where the particle with different impact velocities no longer continues to penetrate the substrate according to Figure 2.4c.

2.5 Conclusions

In this study, the impact of a single B_4C particle on an Al substrate in Al/B_4C composite coatings is numerically simulated to examine the effect of impact velocity, particle size, and matrix porosity on the key particle retention parameters (i.e., penetration depth of the particle, the crater morphology, and plastic deformation (PEEQ) of the contact-surface in the substrate). The summarized key results are:

- Higher impact velocities, larger particles, and greater matrix porosity result in deeper penetration.
- Higher impact velocities and smaller particles lead to higher PEEQ values in the substrate.
- The effect of matrix pore size and depth on the PEEQ value is unclear.
- The partial or complete crush of a pore increases the non-uniform shape of the crater.
- A pore at low impact velocities produces a non-uniform distribution of the plastic strain and causes a complex interplay between penetration depth, contact-surface roughness, and the PEEQ value along the contact-surface in the substrate.

Overall, the results indicate that some porosity in the coating prior to deposition may improve particle retention and, by association, coating quality.

Chapter 3

Concluding remarks

3.1 Implications

This thesis explored the effect of a pore in an Al substrate on important particle retention parameters (e.g., depth of penetration of the particle, crater morphology, and value and localization of plastic strain of the substrate) at different impact velocities and with varying B_4C particle sizes in cold sprayed Al/B_4C coatings. The main implications of this thesis are summarized below:

1. This thesis presents an approach for modeling metal/ceramic cold sprayed composite coatings by taking account into the elastic-plastic behavior of the ceramic particle in order to describe the effect of its fracture and fragmentation on substrate behavior, and, subsequently, particle retention. It follows that a model incorporating ceramic elastic-plastic behavior should be used when modeling the deposition of ceramic particles in order to properly represent the physics of the process.

2. This thesis determines the effect of porosity, particle size, and impact velocity on retention of the ceramic particle in a metallic substrate by studying the penetration depth, the crater morphology, equivalent plastic strain and deformation at the crater surface, and distribution of plastic strain across the contact surface. According to the results, this thesis suggests a strategy for modeling a porous

substrate based on the experimental SEM images in the numerical simulations of cold sprayed processes in order to better understand the deposition process and properties of the PRAMC coatings.

3. This thesis provides an insight into the effect of porosity on the plastic strain localization and distribution of the plastic strain across the crater surface, which is similar to the plastic strain distribution induced by higher velocities; consequently, it recommends taking account into the effect of porosity in the substrate and pre-deposited coatings in the manufacturing process of the Al/B_4C composite coatings and similar ceramic/metal coatings at lower velocities.

3.2 Future Works and Recommendations

To build upon the current work of this thesis, future possible research directions are outlined below in terms of numerical modeling and manufacturing recommendations:

- *Considering an interface model* - The current model considers two distinct material models for the boron carbide particle and aluminum substrate that include the effect of plastic strain rate and plastic deformation under impact loading. In the current paper, the interface response is not captured between the particle and substrate, which may play an important role during an impact event [181]. To augment the model, an interface material model including a contact criterion for dynamic loading [182, 183] can be developed via a user subroutine, or by placing a cohesive layer between the particle and substrate [184].

- *Considering a porous substrate* - This model can be further expanded to a substrate with random pores to predict the behavior of a more realistic substrate based on experimental observations (e.g., SEM images with random pore distribution [39]). The pores in the substrate can be modeled as air or vacuum by developing an user subroutine in Abaqus to determine the effect of the porous substrate on the particle retention parameters.

- *Considering thermal-mechanical effects in the substrate model* - The material model used in this simulation consists of two distinct models for ceramic and metallic materials without considering the effect of temperature change. The high velocity impacts of particles result in increasing the temperature that softens the material and may lead to more extensive plastic deformation [93]. The temperature change in ceramic particles will likely not affect the particle thermal-mechanical response due to their high heat resistance, but temperature will affect the metal substrate behavior.

Bibliography

[1] X. Xie *et al.*, "Al matrix composites fabricated by solid-state cold spray deposition: A critical review," *Journal of Materials Science & Technology*, vol. 86, pp. 20–55, 2021.

[2] X. Xie *et al.*, "Achieving simultaneously improved tensile strength and ductility of a nano-tib2/alsi10mg composite produced by cold spray additive manufacturing," *Composites Part B: Engineering*, vol. 202, p. 108 404, 2020.

[3] S. T. I. Nayim *et al.*, "Effect of cnt and tic hybrid reinforcement on the micro-mechano-tribo behaviour of aluminium matrix composites," *Materials Today: Proceedings*, vol. 21, pp. 1421–1424, 2020.

[4] N. K. Chandla, S. Kant, and M. Goud, "Mechanical, tribological and microstructural characterization of stir cast al-6061 metal/matrix composites—a comprehensive review," *Sādhanā*, vol. 46, pp. 1–38, 2021.

[5] S. Madhusudan, M. M. M. Sarcar, and N. B. R. M. Rao, "Mechanical properties of aluminum-copper (p) composite metallic materials," *Journal of applied research and technology*, vol. 14, no. 5, pp. 293–299, 2016.

[6] S. Thirumalvalavan and N Senthilkumar, "Evaluation of mechanical properties of aluminium alloy (lm25) reinforced with fused silica metal matrix composite," 2019.

[7] J. James, A. R. Annamalai, A Muthuchamy, and C.-P. Jen, "Effect of wettability and uniform distribution of reinforcement particle on mechanical property (tensile) in aluminum metal matrix composite—a review," *Nanomaterials*, vol. 11, no. 9, p. 2230, 2021.

[8] S. Tjong and K. Lau, "Tribological behaviour of sic particle-reinforced copper matrix composites," *Materials Letters*, vol. 43, no. 5-6, pp. 274–280, 2000.

[9] P. Deshpande and R. Lin, "Wear resistance of wc particle reinforced copper matrix composites and the effect of porosity," *Materials Science and Engineering: A*, vol. 418, no. 1-2, pp. 137–145, 2006.

[10] M. Shabani, M. H. Paydar, R. Zamiri, M. Goodarzi, and M. M. Moshksar, "Microstructural and sliding wear behavior of sic-particle reinforced copper matrix composites fabricated by sintering and sinter-forging processes," *Journal of Materials Research and Technology*, vol. 5, no. 1, pp. 5–12, 2016.

[11] R. Wang *et al.*, "Novel selective laser melting processed in-situ tic particle-reinforced ni matrix composite with excellent processability and mechanical properties," *Materials Science and Engineering: A*, vol. 797, p. 140 145, 2020.

[12] H Gül, F Kılıç, S Aslan, A. Alp, and H Akbulut, "Characteristics of electro-co-deposited ni–al2o3 nano-particle reinforced metal matrix composite (mmc) coatings," *Wear*, vol. 267, no. 5-8, pp. 976–990, 2009.

[13] Q.-C. Jiang, X. Li, and H. Wang, "Fabrication of tic particulate reinforced magnesium matrix composites," *Scripta Materialia*, vol. 48, no. 6, pp. 713–717, 2003.

[14] K.-K. Deng, C.-J. Wang, K.-B. Nie, and X.-J. Wang, "Recent research on the deformation behavior of particle reinforced magnesium matrix composite: A review," *Acta Metallurgica Sinica (English Letters)*, vol. 32, pp. 413–425, 2019.

[15] X. Wang *et al.*, "Effect of hot extrusion on the microstructure of a particulate reinforced magnesium matrix composite," *Materials Science and Engineering: A*, vol. 465, no. 1-2, pp. 78–84, 2007.

[16] Y. Nishida, *Introduction to metal matrix composites: fabrication and recycling*. Springer Science & Business Media, 2013.

[17] N. Altinkok and R. Koker, "Modelling of the prediction of tensile and density properties in particle reinforced metal matrix composites by using neural networks," *Materials & design*, vol. 27, no. 8, pp. 625–631, 2006.

[18] G. Munday, J. Hogan, and A. McDonald, "On the microstructure-dependency of mechanical properties and failure of low-pressure cold-sprayed tungsten carbide-nickel metal matrix composite coatings," *Surface and Coatings Technology*, vol. 396, p. 125 947, 2020.

[19] X. Wang, A. Jha, and R. Brydson, "In situ fabrication of al3ti particle reinforced aluminium alloy metal–matrix composites," *Materials Science and Engineering: A*, vol. 364, no. 1-2, pp. 339–345, 2004.

[20] Y. Hu and W. Cong, "A review on laser deposition-additive manufacturing of ceramics and ceramic reinforced metal matrix composites," *Ceramics International*, vol. 44, no. 17, pp. 20 599–20 612, 2018.

[21] Y Pazhouhanfar and B Eghbali, "Microstructural characterization and mechanical properties of tib2 reinforced al6061 matrix composites produced using stir casting process," *Materials Science and Engineering: A*, vol. 710, pp. 172–180, 2018.

[22] P. Han *et al.*, "Modification of cold-sprayed high-entropy alloy particles reinforced aluminum matrix composites via friction stir processing," *Journal of Alloys and Compounds*, vol. 907, p. 164 426, 2022.

[23] T. Peat, A. Galloway, A. Toumpis, P. McNutt, and N. Iqbal, "The erosion performance of particle reinforced metal matrix composite coatings produced by co-deposition cold gas dynamic spraying," *Applied Surface Science*, vol. 396, pp. 1623–1634, 2017.

[24] D. Woo *et al.*, "Synthesis of nanodiamond-reinforced aluminum metal composite powders and coatings using high-energy ball milling and cold spray," *Carbon*, vol. 63, pp. 404–415, 2013.

[25] S. Yin *et al.*, "Advanced diamond-reinforced metal matrix composites via cold spray: Properties and deposition mechanism," *Composites Part B: Engineering*, vol. 113, pp. 44–54, 2017.

[26] K. Yang, W. Li, P. Niu, X. Yang, and Y. Xu, "Cold sprayed aa2024/al2o3 metal matrix composites improved by friction stir processing: Microstructure characterization, mechanical performance and strengthening mechanisms," *Journal of Alloys and Compounds*, vol. 736, pp. 115–123, 2018.

[27] K. Hodder, H Izadi, A. McDonald, and A. Gerlich, "Fabrication of aluminum–alumina metal matrix composites via cold gas dynamic spraying at low pressure followed by friction stir processing," *Materials Science and Engineering: A*, vol. 556, pp. 114–121, 2012.

[28] Q. Shen, Z. Yuan, H. Liu, X. Zhang, Q. Fu, and Q. Wang, "The damage mechanism of 17vol.% sicp/al composite under uniaxial tensile stress," *Materials Science and Engineering: A*, vol. 782, p. 139 274, 2020.

[29] R Balokhonov, V Romanova, and A Kulkov, "Microstructure-based analysis of deformation and fracture in metal-matrix composite materials," *Engineering Failure Analysis*, vol. 110, p. 104 412, 2020.

[30] Y. Ma, Z. Chen, M. Wang, D. Chen, N. Ma, and H. Wang, "High cycle fatigue behavior of the in-situ tib2/7050 composite," *Materials Science and Engineering: A*, vol. 640, pp. 350–356, 2015.

[31] P. Peng *et al.*, "Deformation behavior and damage in B4Cp/6061Al composites: An actual 3D microstructure-based modeling," *Materials Science and Engineering: A*, vol. 781, p. 139 169, 2020.

[32] M Winnicki *et al.*, "Corrosion protection and electrical conductivity of copper coatings deposited by low-pressure cold spraying," *Surface and Coatings Technology*, vol. 318, pp. 90–98, 2017.

[33] H. Assadi, H. Kreye, F Gärtner, and T. Klassen, "Cold spraying–a materials perspective," *Acta Materialia*, vol. 116, pp. 382–407, 2016.

[34] D. B. Miracle and W. Hunt, "Automotive applications of metal matrix composites," *Aluminium Consultant Group Inc*, pp. 1029–1032, 2004.

[35] D. K. Sharma, M. Sharma, and G. Upadhyay, "Boron carbide (B4C) reinforced aluminum matrix composites (AMC)," *Int. J. Innovative Technol. Exploring Eng.*, vol. 9, no. 1, pp. 2194–2203, 2019.

[36] T Zeuner, P Stojanov, P. Sahm, H Ruppert, and A Engels, "Developing trends in disc bralke technology for rail application," *Materials Science and Technology*, vol. 14, no. 9-10, pp. 857–863, 1998.

[37] I. Watson, M. Forster, P. Lee, R. Dashwood, R. Hamilton, and A Chirazi, "Investigation of the clustering behaviour of titanium diboride particles in aluminium," *Composites part A: Applied science and Manufacturing*, vol. 36, no. 9, pp. 1177–1187, 2005.

[38] O. Meydanoglu, B. Jodoin, and E. S. Kayali, "Microstructure, mechanical properties and corrosion performance of 7075 Al matrix ceramic particle reinforced composite coatings produced by the cold gas dynamic spraying process," *Surface and Coatings Technology*, vol. 235, pp. 108–116, 2013.

[39] G. Huang, W. Fu, L. Ma, X. Li, and H. Wang, "Cold spraying B4C particles reinforced aluminium coatings," *Surface Engineering*, vol. 35, no. 9, pp. 772–783, 2019.

[40] A. Loganathan, S. Rengifo, A. F. Hernandez, C. Zhang, and A. Agarwal, "Effect of nanodiamond reinforcement and heat-treatment on microstructure, mechanical and tribological properties of cold sprayed aluminum coating," *Surface and Coatings Technology*, vol. 412, p. 127 037, 2021.

[41] J. Xia, J. J. Lewandowski, and M. A. Willard, "Tension and fatigue behavior of Al-2124A/SiC-particulate metal matrix composites," *Materials Science and Engineering: A*, vol. 770, p. 138 518, 2020.

[42] M. Zubcak, J. Soltes, M. Zimina, T. Weinberger, and N. Enzinger, "Investigation of al-b4c metal matrix composites produced by friction stir additive processing," *Metals*, vol. 11, no. 12, p. 2020, 2021.

[43] N. Panwar and A. Chauhan, "Fabrication methods of particulate reinforced aluminium metal matrix composite-a review," *Materials Today: Proceedings*, vol. 5, no. 2, pp. 5933–5939, 2018.

[44] X Zhang and H Hu, "Solidification of magnesium (AM50A)/vol%. SiCp composite," in *IOP Conference Series: Materials Science and Engineering*, IOP Publishing, vol. 27, 2012, p. 012 023.

[45] M. Moazami-Goudarzi and F. Akhlaghi, "Effect of nanosized SiC particles addition to CP Al and Al–Mg powders on their compaction behavior," *Powder Technology*, vol. 245, pp. 126–133, 2013.

[46] S. Pathak and G. C. Saha, *Cold Spray in the Realm of Additive Manufacturing*. Springer, 2020.

[47] C Saravanan, K Subramanian, V. A. Krishnan, and R. S. Narayanan, "Effect of particulate reinforced aluminium metal matrix composite–a review," *Mechanics and Mechanical Engineering*, vol. 19, no. 1, pp. 23–30, 2015.

[48] P. Han *et al.*, "Friction stir processing of cold-sprayed high-entropy alloy particles reinforced aluminum matrix composites: Corrosion and wear properties," *Metals and Materials International*, pp. 1–16, 2022.

[49] S. R. Bakshi, V. Singh, K. Balani, D. G. McCartney, S. Seal, and A. Agarwal, "Carbon nanotube reinforced aluminum composite coating via cold spraying," *Surface and Coatings Technology*, vol. 202, no. 21, pp. 5162–5169, 2008.

[50] X. Xie *et al.*, "Recent developments in solid-state cold spraying of al matrix composites: A critical review," *Journal of Materials Science and Technology*, vol. 86, pp. 20–55, 2021.

[51] L. He and M. Hassani, "A review of the mechanical and tribological behavior of cold spray metal matrix composites," *Journal of Thermal Spray Technology*, vol. 29, no. 7, pp. 1565–1608, 2020.

[52] P Richer, A Zúñiga, M Yandouzi, and B Jodoin, "Conicraly microstructural changes induced during cold gas dynamic spraying," *Surface and Coatings Technology*, vol. 203, no. 3-4, pp. 364–371, 2008.

[53] X. Zhou, A. Chen, J. Liu, X. Wu, and J. Zhang, "Preparation of metallic coatings on polymer matrix composites by cold spray," *Surface and Coatings Technology*, vol. 206, no. 1, pp. 132–136, 2011.

[54] H.-J. Kim, C.-H. Lee, and S.-Y. Hwang, "Fabrication of wc–co coatings by cold spray deposition," *Surface and Coatings Technology*, vol. 191, no. 2-3, pp. 335–340, 2005.

[55] X.-T. Luo, C.-X. Li, F.-L. Shang, G.-J. Yang, Y.-Y. Wang, and C.-J. Li, "High velocity impact induced microstructure evolution during deposition of cold spray coatings: A review," *Surface and Coatings Technology*, vol. 254, pp. 11–20, 2014.

[56] M. Winnicki, "Advanced functional metal-ceramic and ceramic coatings deposited by low-pressure cold spraying: A review," *Coatings*, vol. 11, no. 9, p. 1044, 2021.

[57] M Yu, X. Suo, W. Li, Y. Wang, and H. Liao, "Microstructure, mechanical property and wear performance of cold sprayed al5056/sicp composite coatings: Effect of reinforcement content," *Applied surface science*, vol. 289, pp. 188–196, 2014.

[58] T. Norrell, G. Ferguson, T. Ansell, T. Saladin, A. Nardi, and A. Nieto, "Synthesis and corrosion behavior of cold sprayed dual nanoparticle reinforced al coatings," *Surface and Coatings Technology*, vol. 401, p. 126 280, 2020.

[59] C. Huang, W. Li, Z. Zhang, M.-p. Planche, H. Liao, and G. Montavon, "Effect of tool rotation speed on microstructure and microhardness of friction-stir-processed cold-sprayed sicp/al5056 composite coating," *Journal of Thermal Spray Technology*, vol. 25, pp. 1357–1364, 2016.

[60] C. Wu *et al.*, "Influence of particle size and spatial distribution of b4c reinforcement on the microstructure and mechanical behavior of precipitation strengthened al alloy matrix composites," *Materials Science and Engineering: A*, vol. 675, pp. 421–430, 2016.

[61] S. I. Imbriglio and R. R. Chromik, "Factors affecting adhesion in metal/ceramic interfaces created by cold spray," *Journal of Thermal Spray Technology*, vol. 30, no. 7, pp. 1703–1723, 2021.

[62] X. Qiu, J.-q. Wang, J.-r. Tang, L. Gyansah, Z.-p. Zhao, T.-y. Xiong, *et al.*, "Microstructure, microhardness and tribological behavior of al2o3 reinforced a380 aluminum alloy composite coatings prepared by cold spray technique," *Surface and Coatings Technology*, vol. 350, pp. 391–400, 2018.

[63] H. Kwon, S. Cho, and A. Kawasaki, "Diamond-reinforced metal matrix bulk materials fabricated by a low-pressure cold-spray process," *Materials Transactions*, vol. 56, no. 1, pp. 108–112, 2015.

[64] Q. Wang, K. Spencer, N. Birbilis, and M.-X. Zhang, "The influence of ceramic particles on bond strength of cold spray composite coatings on AZ91 alloy substrate," *Surface and Coatings Technology*, vol. 205, no. 1, pp. 50–56, 2010.

[65] E. Bakan, D. Marcano, D. Zhou, Y. J. Sohn, G. Mauer, and R. Vaßen, "Yb2Si2O7 environmental barrier coatings deposited by various thermal spray techniques: a preliminary comparative study," *Journal of thermal spray technology*, vol. 26, no. 6, pp. 1011–1024, 2017.

[66] J. K. Penney, *Cold Spray of Copper onto Niobium for Conductive Cooling of Superconducting Radio Frequency Structures*. University of California, Los Angeles, 2020.

[67] L. Zhao *et al.*, "Effect of particle size on ceramic particle content in cold sprayed Al-Based metal matrix composite coating," *Journal of Thermal Spray Technology*, pp. 1–12, 2022.

[68] L. Zhao *et al.*, "Unraveling the influence of al particle size on microstructure and tribological properties of cold sprayed al/b4c composite coatings," *Materials Today Communications*, vol. 34, p. 105 257, 2023.

[69] T. Ye, Y. Xu, and J. Ren, "Effects of sic particle size on mechanical properties of sic particle reinforced aluminum metal matrix composite," *Materials Science and Engineering: A*, vol. 753, pp. 146–155, 2019.

[70] R. Fernandez and B. Jodoin, "Cold spray aluminum–alumina cermet coatings: effect of alumina content," *Journal of thermal spray technology*, vol. 27, no. 4, pp. 603–623, 2018.

[71] V. Shikalov, V. Kosarev, T. Vidyuk, S. Klinkov, and I. Batraev, "Mechanical and tribological properties of cold sprayed composite Al-B4C coatings," in *AIP Conference Proceedings*, AIP Publishing LLC, vol. 2448, 2021, p. 020 021.

[72] G. V. Kumar, C. Rao, N Selvaraj, *et al.*, "Mechanical and tribological behavior of particulate reinforced aluminum metal matrix composites–a review," *Journal of minerals and materials characterization and engineering*, vol. 10, no. 01, p. 59, 2011.

[73] J. M. Shockley, S. Descartes, P Vo, E. Irissou, and R. Chromik, "The influence of al2o3 particle morphology on the coating formation and dry sliding wear behavior of cold sprayed al–al2o3 composites," *Surface and Coatings Technology*, vol. 270, pp. 324–333, 2015.

[74] S. I. Imbriglio, *Mechanisms and parameters affecting adhesion for titanium/ceramic interfaces created by cold spray*. McGill University (Canada), 2020.

[75] Y. T. R. Lee, H. Ashrafizadeh, G. Fisher, and A. McDonald, "Effect of type of reinforcing particles on the deposition efficiency and wear resistance of low-pressure cold-sprayed metal matrix composite coatings," *Surface and Coatings Technology*, vol. 324, pp. 190–200, 2017.

[76] V. Shikalov, T. Vidyuk, V. Kosarev, and S. Klinkov, "Effect of b4c content on microhardness and sliding wear behavior of cold sprayed aluminum matrix coatings," in *AIP Conference Proceedings*, AIP Publishing LLC, vol. 2351, 2021, p. 040 060.

[77] R. Chakrabaarty and J. Song, "Effect of impact angle on ceramic deposition behavior in composite cold spray: A finite-element study," *Journal of Thermal Spray Technology*, vol. 26, no. 7, pp. 1434–1444, 2017.

[78] A. Elkin, A Lama, S Dautov, and P Shornikov, "Numerical study of ceramic retention mechanism in cold spraying," in *ITSC2022*, ASM International, 2022, pp. 990–999.

[79] R. Chakrabarty and J. Song, "Numerical simulations of ceramic deposition and retention in metal-ceramic composite cold spray," *Surface and Coatings Technology*, vol. 385, p. 125 324, 2020.

[80] W. Li, K. Yang, D. Zhang, and X. Zhou, "Residual stress analysis of cold-sprayed copper coatings by numerical simulation," *Journal of Thermal Spray Technology*, vol. 25, no. 1, pp. 131–142, 2016.

[81] A. A. Lordejani, L. Vitali, M. Guagliano, and S. Bagherifard, "Estimating deposition efficiency and chemical composition variation along thickness for cold spraying of composite feedstocks," *Surface and Coatings Technology*, vol. 436, p. 128 239, 2022.

[82] M. Terrone, A. A. Lordejani, J. Kondas, and S. Bagherifard, "A numerical approach to design and develop freestanding porous structures through cold spray multi-material deposition," *Surface and Coatings Technology*, vol. 421, p. 127 423, 2021.

[83] X. Song *et al.*, "Coupled eulerian-lagrangian (cel) simulation of multiple particle impact during metal cold spray process for coating porosity prediction," *Surface and Coatings Technology*, vol. 385, p. 125 433, 2020.

[84] S. Weiller and F. Delloro, "A numerical study of pore formation mechanisms in aluminium cold spray coatings," *Additive Manufacturing*, vol. 60, p. 103 193, 2022.

[85] S. Yin, X.-f. Wang, B.-p. Xu, and W.-y. Li, "Examination on the calculation method for modeling the multi-particle impact process in cold spraying," *Journal of thermal spray technology*, vol. 19, no. 5, pp. 1032–1041, 2010.

[86] X. Song *et al.*, "Residual stresses in single particle splat of metal cold spray process–numerical simulation and direct measurement," *Materials Letters*, vol. 230, pp. 152–156, 2018.

[87] R. Ghelichi, S. Bagherifard, D MacDonald, I. Fernandez-Pariente, B Jodoin, and M. Guagliano, "Experimental and numerical study of residual stress evolution in cold spray coating," *Applied Surface Science*, vol. 288, pp. 26–33, 2014.

[88] J. M. Schreiber, *Finite Element Implementation of the Preston-Tonks-Wallace Plasticity Model and Energy Based Bonding Parameter for the Cold Spray Process*. The Pennsylvania State University, 2016.

[89] T. Schmidt, F. Gärtner, H. Assadi, and H. Kreye, "Development of a generalized parameter window for cold spray deposition," *Acta materialia*, vol. 54, no. 3, pp. 729–742, 2006.

[90] G. Qiu, S. Henke, and J. Grabe, "Application of a coupled eulerian–lagrangian approach on geomechanical problems involving large deformations," *Computers and Geotechnics*, vol. 38, no. 1, pp. 30–39, 2011.

[91] Z. Zhu, S. Kamnis, and S. Gu, "Numerical study of molten and semi-molten ceramic impingement by using coupled eulerian and lagrangian method," *Acta Materialia*, vol. 90, pp. 77–87, 2015.

[92] S. Weiller, F. Delloro, P. Lomonaco, M. Jeandin, and C. Garion, "A finite elements study on porosity creation mechanisms in cold sprayed coatings," in *Key Engineering Materials*, Trans Tech Publ, vol. 813, 2019, pp. 358–363.

[93] J. Xie, D. Nélias, W.-L. Berre, K. Ogawa, Y. Ichikawa, *et al.*, "Simulation of the cold spray particle deposition process," *Journal of Tribology*, vol. 137, no. 4, 2015.

[94] W.-Y. Li, C. Zhang, C.-J. Li, and H. Liao, "Modeling aspects of high velocity impact of particles in cold spraying by explicit finite element analysis," *Journal of Thermal Spray Technology*, vol. 18, no. 5, pp. 921–933, 2009.

[95] B. Yildirim, S. Muftu, and A. Gouldstone, "Modeling of high velocity impact of spherical particles," *Wear*, vol. 270, no. 9-10, pp. 703–713, 2011.

[96] G Shayegan *et al.*, "Residual stress induced by cold spray coating of magnesium AZ31B extrusion," *Materials & Design*, vol. 60, pp. 72–84, 2014.

[97] J.-G. Lee *et al.*, "Thin film metallization by supersonic spraying of copper and nickel nanoparticles on a silicon substrate," *Computational Materials Science*, vol. 108, pp. 114–120, 2015.

[98] D MacDonald, R Fernández, F Delloro, and B Jodoin, "Cold spraying of armstrong process titanium powder for additive manufacturing," *Journal of Thermal Spray Technology*, vol. 26, no. 4, pp. 598–609, 2017.

[99] G. Bae, Y. Xiong, S Kumar, K. Kang, and C. Lee, "General aspects of interface bonding in kinetic sprayed coatings," *Acta Materialia*, vol. 56, no. 17, pp. 4858–4868, 2008.

[100] W.-Y. Li, H. Liao, C.-J. Li, G. Li, C. Coddet, and X. Wang, "On high velocity impact of micro-sized metallic particles in cold spraying," *Applied surface science*, vol. 253, no. 5, pp. 2852–2862, 2006.

[101] F. Delloro *et al.*, "A morphological approach to the modeling of the cold spray process," *Journal of Thermal Spray Technology*, vol. 26, no. 8, pp. 1838–1850, 2017.

[102] M. Saleh, V. Luzin, and K. Spencer, "Analysis of the residual stress and bonding mechanism in the cold spray technique using experimental and numerical methods," *Surface and Coatings Technology*, vol. 252, pp. 15–28, 2014.

[103] A. Manap, K. Ogawa, and T. Okabe, "Numerical analysis of interfacial bonding of al-si particle and mild steel substrate by cold spray technique using the sph method," *Journal of Solid Mechanics and Materials Engineering*, vol. 6, no. 3, pp. 241–250, 2012.

[104] A. Manap, O Nooririnah, H Misran, T Okabe, and K Ogawa, "Experimental and sph study of cold spray impact between similar and dissimilar metals," *Surface Engineering*, vol. 30, no. 5, pp. 335–341, 2014.

[105] G. R. Johnson, "A constitutive model and data for materials subjected to large strains, high strain rates, and high temperatures," *Proc. 7th Inf. Sympo. Ballistics*, pp. 541–547, 1983.

[106] R. Menikoff, "Complete Mie-Gruneisen equation of state (update)," Los Alamos National Lab.(LANL), Los Alamos, NM (United States), Tech. Rep., 2016.

[107] R. Chakrabarty and J. Song, "A modified johnson-cook material model with strain gradient plasticity consideration for numerical simulation of cold spray process," *Surface and Coatings Technology*, vol. 397, p. 125 981, 2020.

[108] R. Chakrabarty and J. Song, "Numerical modeling of fracture in ceramic micro-particles and insights on ceramic retention during composite cold spray process," *Surface and Coatings Technology*, vol. 409, p. 126 830, 2021.

[109] M Fouad, "Aluminium+ boron carbide cold sprayed coatings," in *-2021*, 2021, pp. 165–165.

[110] V. Tvergaard and A. Needleman, "Analysis of the cup-cone fracture in a round tensile bar," *Acta metallurgica*, vol. 32, no. 1, pp. 157–169, 1984.

[111] T. J. Holmquist and G. R. Johnson, "Characterization and evaluation of silicon carbide for high-velocity impact," *Journal of applied physics*, vol. 97, no. 9, p. 093 502, 2005.

[112] H. Assadi, F. Gärtner, T. Stoltenhoff, and H. Kreye, "Bonding mechanism in cold gas spraying," *Acta materialia*, vol. 51, no. 15, pp. 4379–4394, 2003.

[113] G. R. Johnson and T. J. Holmquist, "An improved computational constitutive model for brittle materials," in *AIP conference proceedings*, American Institute of Physics, vol. 309, 1994, pp. 981–984.

[114] T. Holmquist and G. Johnson, "Response of boron carbide subjected to high-velocity impact," *International Journal of Impact Engineering*, vol. 35, no. 8, pp. 742–752, 2008.

[115] R. Scazzosi, M. Giglio, and A. Manes, "Fe coupled to sph numerical model for the simulation of high-velocity impact on ceramic based ballistic shields," *Ceramics International*, vol. 46, no. 15, pp. 23 760–23 772, 2020.

[116] L. M. Bresciani, A. Manes, T. Romano, P Iavarone, and M. Giglio, "Numerical modelling to reproduce fragmentation of a tungsten heavy alloy projectile impacting a ceramic tile: Adaptive solid mesh to the sph technique and the cohesive law," *International Journal of Impact Engineering*, vol. 87, pp. 3–13, 2016.

[117] J. Cao, Y. Wu, J. Li, and Q. Zhang, "Study on the material removal process in ultrasonic-assisted grinding of sic ceramics using smooth particle hydrodynamic (sph) method," *The International Journal of Advanced Manufacturing Technology*, vol. 83, no. 5-8, pp. 985–994, 2016.

[118] G. Guo, S. Alam, and L. D. Peel, "Numerical analysis of ballistic impact performance of two ceramic-based armor structures," *Composites Part C: Open Access*, vol. 3, p. 100 061, 2020.

[119] A. Chesnokov, A. Smirnov, S. Klinkov, and V. Kosarev, "Preparation of the composite powder al–b4c by ball milling for cold spray," in *Journal of Physics: Conference Series*, IOP Publishing, vol. 1945, 2021, p. 012 033.

[120] L. Gyansah *et al.*, "Achieving strength-ductility synergy in cold spray additively manufactured al/b4c composites through a hybrid post-deposition treatment," *Journal of Materials Science & Technology*, vol. 35, no. 6, pp. 1053–1063, 2019.

[121] T. Vidyuk, V. Kosarev, S. Klinkov, and V. Shikalov, "Properties of cold sprayed composite metal+ b4c coatings," in *AIP Conference Proceedings*, AIP Publishing LLC, vol. 2125, 2019, p. 030 025.

[122] K. R. Chang, V Rubanik, and V Rubanik jr, "Cold gas-dynamic spraying coatings based on aluminum with boron carbide addition," in *60 " "*, 2018, pp. 556–557.

[123] C. Shao, C. Lo, K. Bhagavathula, A. McDonald, and J. Hogan, "High strength particulate aluminum matrix composite design: Synergistic strengthening strategy," *Composites Communications*, vol. 25, p. 100 697, 2021.

[124] S. Sayahlatifi, C. Shao, A. McDonald, and J. Hogan, "3D microstructure-based finite element simulation of cold-sprayed Al-Al2O3 composite coatings under quasi-static compression and indentation loading," *Journal of Thermal Spray Technology*, pp. 1–17, 2021.

[125] B. Teng, W. Wang, Y. Liu, and S. Yuan, "Bursting prediction of hydroforming aluminium alloy tube based on Gurson-Tvergaard-Needleman damage model," *Procedia Engineering*, vol. 81, pp. 2211–2216, 2014.

[126] T. Holmquist and G. Johnson, "Characterization and evaluation of boron carbide for plate-impact conditions," *Journal of applied physics*, vol. 100, no. 9, p. 093 525, 2006.

[127] V. Champagne and D. Helfritch, "Mainstreaming cold spray–push for applications," *Surface Engineering*, vol. 30, no. 6, pp. 396–403, 2014.

[128] S. Spath and H. Seitz, "Influence of grain size and grain-size distribution on workability of granules with 3d printing," *The International Journal of Advanced Manufacturing Technology*, vol. 70, no. 1-4, pp. 135–144, 2014.

[129] T Yang, M Yu, H Chen, W. Li, and H. Liao, "Characterisation of cold sprayed Al5056/SiCp coating: effect of SiC particle size," *Surface Engineering*, vol. 32, no. 9, pp. 641–649, 2016.

[130] Q. Wang, N. Birbilis, H. Huang, and M.-X. Zhang, "Microstructure characterization and nanomechanics of cold-sprayed pure Al and Al-Al2O3 composite coatings," *Surface and Coatings Technology*, vol. 232, pp. 216–223, 2013.

[131] C. Kuang *et al.*, "Boosting photocatalytic interaction of sulphur doped reduced graphene oxide-based s@ rgo/nis2 nanocomposite for destruction of pathogens and organic pollutant degradation caused by visible light," *Inorganic Chemistry Communications*, vol. 141, p. 109 575, 2022.

[132] S. M. Javed *et al.*, "Highly dispersed active sites of ni nanoparticles onto hierarchical reduced graphene oxide architecture towards efficient water oxidation," *Fuel*, vol. 312, p. 122 926, 2022.

[133] B. Torres, M. A. Garrido, A. Rico, P Rodrigo, M. Campo, and J Rams, "Wear behaviour of thermal spray Al/SiCp coatings," *Wear*, vol. 268, no. 5-6, pp. 828–836, 2010.

[134] P. Cavaliere, L Cavaliere, and Lekhwani, *Cold-spray coatings*. Springer, 2018.

[135] B. Wielage, T. Grund, C. Rupprecht, and S Kuemmel, "New method for producing power electronic circuit boards by cold-gas spraying and investigation of adhesion mechanisms," *Surface and Coatings Technology*, vol. 205, no. 4, pp. 1115–1118, 2010.

[136] A.-M. Bandar, R. Mongrain, E. Irissou, and S. Yue, "Improving the strength and corrosion resistance of 316l stainless steel for biomedical applications using cold spray," *Surface and Coatings Technology*, vol. 216, pp. 297–307, 2013.

[137] A. Moridi, S. M. Hassani-Gangaraj, M. Guagliano, and M. Dao, "Cold spray coating: Review of material systems and future perspectives," *Surface Engineering*, vol. 30, no. 6, pp. 369–395, 2014.

[138] Q. Wang *et al.*, "The influence of cold and detonation thermal spraying processes on the microstructure and properties of Al-based composite coatings on Mg alloy," *Surface and Coatings Technology*, vol. 352, pp. 627–633, 2018.

[139] V. K. Pandey, B. P. Patel, and S. Guruprasad, "Mechanical properties of Al/Al2O3 and Al/B4C composites," *Advances in materials Research*, vol. 5, no. 4, p. 263, 2016.

[140] S. W. Glass *et al.*, "Cold spray nde for porosity and other process anomalies," in *AIP Conference Proceedings*, AIP Publishing LLC, vol. 1949, 2018, p. 020 010.

[141] A. A. Lordejani, D Colzani, M Guagliano, and S Bagherifard, "An inclusive numerical framework to assess the role of feedstock features on the quality of cold spray deposits," *Materials & Design*, vol. 224, p. 111 374, 2022.

[142] J. Schreiber, I Smid, T. Eden, K Koudela, D Cote, and V Champagne, "Cold spray particle impact simulation using the preston-tonks-wallace plasticity model," *Finite Elements in Analysis and Design*, vol. 191, p. 103 557, 2021.

[143] R. Yildiz and S Yilmaz, "Experimental investigation of GTN model parameters of 6061 Al alloy," *European Journal of Mechanics-A/Solids*, vol. 83, p. 104 040, 2020.

[144] A. Lamberts, M. Geers, J. van Dommelen, H. de Lange, A. Huizinga, and P. BV, "Numerical simulation of ballistic impacts on ceramic material," *Nederland: Eindhoven University of Technology*, 2007.

[145] W.-Y. Li, H. Liao, C.-J. Li, H.-S. Bang, and C Coddet, "Numerical simulation of deformation behavior of Al particles impacting on Al substrate and effect of surface oxide films on interfacial bonding in cold spraying," *Applied Surface Science*, vol. 253, no. 11, pp. 5084–5091, 2007.

[146] N. Benseddiq and A. Imad, "A ductile fracture analysis using a local damage model," *International Journal of Pressure Vessels and Piping*, vol. 85, no. 4, pp. 219–227, 2008.

[147] M. C. Schaefer and R. A. Haber, "Amorphization mitigation in boron-rich boron carbides quantified by raman spectroscopy," *Ceramics*, vol. 3, no. 3, pp. 297–305, 2020.

[148] G. R. Johnson, T. J. Holmquist, and S. R. Beissel, "Response of aluminum nitride (including a phase change) to large strains, high strain rates, and high pressures," *Journal of Applied Physics*, vol. 94, no. 3, pp. 1639–1646, 2003.

[149] H Assadi, T Klassen, F Gartner, *et al.*, "Modelling of impact and bonding of inhomogeneous particles in cold spraying," in *International thermal spray conference, Barcelona*, 2014, pp. 21–23.

[150] G. Bae *et al.*, "Bonding features and associated mechanisms in kinetic sprayed titanium coatings," *Acta Materialia*, vol. 57, no. 19, pp. 5654–5666, 2009.

[151] A. Fardan and R. Ahmed, "Modeling the evolution of residual stresses in thermally sprayed YSZ coating on stainless steel substrate," *Journal of Thermal Spray Technology*, vol. 28, no. 4, pp. 717–736, 2019.

[152] H. ABAQUS, "Abaqus standard user's manual, version 6.14," *Providence, RI, USA: Dassault Systèmes*, 2014.

[153] P. Nicewicz, P. Peciar, O. Macho, T. Sano, and J. D. Hogan, "Quasi-static confined uniaxial compaction of granular alumina and boron carbide observing the particle size effects," *Journal of the American Ceramic Society*, vol. 103, no. 3, pp. 2193–2209, 2020.

[154] D. S. S. Crop, *Abaqus 6.10 example problems manual vollume ii: Other applications and analyses*, 2010.

[155] T. Irvine, "Damping properties of materials," *Magnesium*, vol. 5000, no. 3100, pp. 10–14, 2004.

[156] B. Bhushan, *Introduction to tribology*. John Wiley & Sons, 2013.

[157] S. Rahmati and B. Jodoin, "Physically based finite element modeling method to predict metallic bonding in cold spray," *Journal of Thermal Spray Technology*, vol. 29, pp. 611–629, 2020.

[158] L. Zhu, T.-C. Jen, Y.-T. Pan, and H.-S. Chen, "Particle bonding mechanism in cold gas dynamic spray: A three-dimensional approach," *Journal of Thermal Spray Technology*, vol. 26, pp. 1859–1873, 2017.

[159] B. A. Chalmers, "Defence research establishment center de recherches pour la defense Valcatier, Quebec," 1998.

[160] M. Hassani-Gangaraj, D. Veysset, V. K. Champagne, K. A. Nelson, and C. A. Schuh, "Adiabatic shear instability is not necessary for adhesion in cold spray," *Acta Materialia*, vol. 158, pp. 430–439, 2018.

[161] A. Documentation and U Manual, "Version 6.14, simulia, dassault systèmes.(2015)," *Google Scholar*,

[162] N. K. Singh, K. Z. Uddin, J. Muthulingam, R. Jha, and B. Koohbor, "A modeling study of bonding mechanisms between similar and dissimilar materials in cold spraying on polymeric substrates," *Journal of Thermal Spray Technology*, pp. 1–17, 2022.

[163] W. K. W. Tai *et al.*, "Comparing relative bond characteristics between spherical and elongated morphologies for cold spray process using SPH simulation," *Journal of Thermal Spray Technology*, pp. 1–16, 2022.

[164] J. Ma, J. Chen, J. Guan, Y. Lin, W. Chen, and L. Huang, "Implementation of Johnson-Holmquist-Beissel model in four-dimensional lattice spring model and its application in projectile penetration," *International Journal of Impact Engineering*, vol. 170, p. 104 340, 2022.

[165] M. R. I. Islam, J. Zheng, and R. C. Batra, "Ballistic performance of ceramic and ceramic-metal composite plates with JH1, JH2 and JHB material models," *International Journal of Impact Engineering*, vol. 137, p. 103 469, 2020.

[166] W. Tillmann, M. Abdulgader, L. Hagen, and S. Hüning, "Embedding behavior of ceramic particles in babbitt coatings and its effect on the tribological properties of low-pressure cold sprayed coatings," *Coatings*, vol. 10, no. 8, p. 769, 2020.

[167] A Shkodkin, A Kashirin, O Klyuev, and T Buzdygar, "Metal particle deposition stimulation by surface abrasive treatment in gas dynamic spraying," *Journal of Thermal Spray Technology*, vol. 15, no. 3, pp. 382–386, 2006.

[168] J. Miguel, J. Guilemany, and S Dosta, "Effect of the spraying process on the microstructure and tribological properties of bronze–alumina composite coatings," *Surface and Coatings Technology*, vol. 205, no. 7, pp. 2184–2190, 2010.

[169] M. Hassani-Gangaraj, D. Veysset, K. A. Nelson, and C. A. Schuh, "In-situ observations of single micro-particle impact bonding," *Scripta Materialia*, vol. 145, pp. 9–13, 2018.

[170] T. Schmidt *et al.*, "From particle acceleration to impact and bonding in cold spraying," *Journal of thermal spray technology*, vol. 18, no. 5, pp. 794–808, 2009.

[171] A Sova, V. Kosarev, A Papyrin, and I Smurov, "Effect of ceramic particle velocity on cold spray deposition of metal-ceramic coatings," *Journal of thermal spray technology*, vol. 20, no. 1, pp. 285–291, 2011.

[172] M. Yu, H. Saito, C. Bernard, Y. Ichikawa, and K. Ogawa, "Influence of the low-pressure cold spray operation parameters on coating properties in metallization of ceramic substrates using copper and aluminum composite powder," in *ITSC2021*, ASM International, 2021, pp. 147–152.

[173] M. Yu, Y. Ichikawa, and K. Ogawa, "Development of cu coating on ceramic substrates by low pressure cold spray and its deposition mechanism analysis," in *Materials Science Forum*, Trans Tech Publ, vol. 1016, 2021, pp. 1703–1709.

[174] O. Tregenza, M. Saha, N. Hutasoit, C. Hulston, and S. Palanisamy, "An experimental evaluation of the thermal interface resistance between cold sprayed copper/laser-textured alumina bi-layered composites," *International Journal of Heat and Mass Transfer*, vol. 188, p. 122 606, 2022.

[175] W. Li, C. Cao, and S. Yin, "Solid-state cold spraying of ti and its alloys: A literature review," *Progress in Materials Science*, vol. 110, p. 100 633, 2020.

[176] H. Singh, T. Sidhu, and S. Kalsi, "Cold spray technology: Future of coating deposition processes," *Frattura ed Integrità Strutturale*, vol. 6, no. 22, pp. 69–84, 2012.

[177] X.-J. Ning, J.-H. Jang, and H.-J. Kim, "The effects of powder properties on in-flight particle velocity and deposition process during low pressure cold spray process," *Applied Surface Science*, vol. 253, no. 18, pp. 7449–7455, 2007.

[178] C.-J. Li, W.-Y. Li, and H. Liao, "Examination of the critical velocity for deposition of particles in cold spraying," *Journal of Thermal Spray Technology*, vol. 15, no. 2, pp. 212–222, 2006.

[179] M Yu, W.-Y. Li, X. Suo, and H. Liao, "Effects of gas temperature and ceramic particle content on microstructure and microhardness of cold sprayed SiCp/Al 5056 composite coatings," *Surface and Coatings Technology*, vol. 220, pp. 102–106, 2013.

[180] H Lee and K Ko, "Fabrication of porous Al alloy coatings by cold gas dynamic spray process," *Surface engineering*, vol. 26, no. 6, pp. 395–398, 2010.

[181] A. Hemeda *et al.*, "Particle-based simulation of cold spray: Influence of oxide layer on impact process," *Additive Manufacturing*, vol. 37, p. 101 517, 2021.

[182] Z. Zhang *et al.*, "SPH modeling and investigation of cold spray additive manufacturing with multi-layer multi-track powders," *Journal of Manufacturing Processes*, vol. 84, pp. 565–586, 2022.

[183] R. Melentiev, A. Yudhanto, R. Tao, T. Vuchkov, and G. Lubineau, "Metallization of polymers and composites: State-of-the-art approaches," *Materials & Design*, p. 110 958, 2022.

[184] P Cavaliere and A Silvello, "Crack repair in aerospace aluminum alloy panels by cold spray," *Journal of Thermal Spray Technology*, vol. 26, pp. 661–670, 2017.